A Bioluminescent Activity Dependent (BLADe) Platform for Converting Intracellular Activity to Photoreceptor Activation

Emmanuel L. Crespo[1,2]†, Akash Pal[1,3]†, Mansi Prakash[1], Alexander D. Silvagnoli[1,3], Zohair Zaidi[4], Manuel Gomez-Ramirez[5], Maya O. Tree[1], Nathan C. Shaner[6], Diane Lipscombe[5,7], Christopher I. Moore[5,7]*, Ute Hochgeschwender[1-3]*

[1] College of Medicine, Central Michigan University, Mount Pleasant, MI 48859, USA
[2] Biochemistry, Cell and Molecular Biology Graduate Program, Central Michigan University, Mount Pleasant, MI 48859, USA
[3] Program in Neuroscience, Central Michigan University, Mount Pleasant, MI 48859, USA
[4] Duke University, Undergraduate Neuroscience Program, Durham, NC 27710
[5] Department of Neuroscience, Brown University, Providence, RI 02912, USA
[6] University of California, San Diego, School of Medicine, Department of Neuroscience, 9500 Gilman Drive La Jolla, CA 92093-0662, USA
[7] Carney Institute for Brain Science, Brown University, Providence, RI 02906, USA

†These authors contributed equally to this work: Emmanuel L. Crespo and Akash Pal
*Corresponding authors: Ute Hochgeschwender (hochg1u@cmich.edu) and Christopher I. Moore (christopher_moore@brown.edu)

Abstract

Genetically encoded sensors and actuators have advanced the ability to observe and manipulate cellular activity, yet few non-invasive strategies enable cells to directly couple their intracellular states to user-defined outputs. We developed a bioluminescent activity-dependent (BLADe) platform that facilitates programmable feedback through genetically encoded light generation. Using calcium (Ca^{2+}) flux as a model, we engineered a Ca^{2+}-dependent luciferase that functions as both a reporter and an activity-gated light source capable of photoactivating light-sensing actuators. In neurons, the presence of luciferin triggers Ca^{2+} dependent local illumination that provides activity dependent gene expression by activating a light-sensitive transcription factor and control of neural dynamics through opsin activation in single cells, populations and intact tissue. BLADe can be expanded to couple any signal that bioluminescent enzymes can be engineered to detect with the wide variety of photosensing actuators. This modular strategy of coupling an activity dependent light emitter to a light sensing actuator offers a generalizable framework for state dependent cell-autonomous control across biological systems.

Introduction

Bioluminescence, the emission of light generated when a luciferase enzyme oxidizes a small molecule luciferin, served as a non-invasive approach for *in vitro* and *in vivo* imaging for decades[1]. More recently, with the development of brighter, blue light emitting luciferases in combination with light sensing elements, including opsins and non-opsin photoreceptors[2,3], transformed bioluminescence from a mere imaging reagent to a versatile tool for controlling molecular processes. We and others have combined luciferases with channelrhodopsins and pumps for bioluminescence-driven changes in membrane potential[4–6], light-sensing transcription factors for gene expression[7–9], light-sensing enzymes for cAMP production[10], as well as with genetically encoded photosensitizers for reactive oxygen species production[11,12]. The main advantages of using locally produced bioluminescence rather than external light sources for activating photoreceptors are the independence from optical fiber implants, thereby avoiding the physical

damage to cells as well as the limitation in the number of cells that can be simultaneously controlled.

We now are exploring a unique feature of employing genetically encoded light emitters. By engineering the luciferase protein to accommodate sensor moieties, light emission can be made dependent on the presence of various intracellular agents that report a cell's state. Several such bioluminescent sensors have been developed for reporting intracellular biochemical signals, such as intracellular Ca^{2+}, ATP, or cAMP, including for imaging studies *in vivo*[13]. Here, we are combining a bioluminescent sensor with light-dependent actuators to create an integrator, opening a general platform for converting biochemical signals within cells into photoreceptor activation and resulting downstream changes in cellular function. This Bioluminescence Activity Dependent (BLADe) paradigm serves to integrate cellular activity states with downstream consequences from transcription to membrane potential changes, depending on the optogenetic actuator coupled to the conditional luciferase. By engineering luciferases to respond to specific biochemical cues, this framework can, in principle, be extended to a broad range of intracellular states depending on the sensor domain used. Any bioluminescence indicator can be transformed from a sensor into an activity integrator by using its light emission to activate photoreceptors.

To validate this experimental framework, we developed a BLADe platform based on intracellular calcium level fluctuations. Changes in Ca^{2+} levels are directly translated into bioluminescence light emission by making light production dependent on Ca^{2+} binding in a split luciferase construct. The Ca^{2+} dependent light emitter was paired with a light-dependent transcription factor that detected this light and affected transcription *in vitro* and *in vivo*. Moreover, when paired with channelrhodopsins Ca^{2+} dependent light emission enabled neural activity-driven change in firing activity *in vitro* in single neurons and neuronal populations; in mice, BLADe converted spontaneous activity and sensory evoked changes into activity dependent control of neocortical network dynamics.

Results

Engineering of a luciferase-based Ca^{2+} sensor

The *Gaussia princeps* luciferase variant sbGLuc is an efficient transmitter of photons/energy to opsin chromophores when tethered to opsins in luminopsins[5,14]. To make it Ca^{2+} dependent we split sbGLuc as was done previously for wildtype GLuc between Q88 and G89[15] and introduced the Ca^{2+} sensing moiety CaM-M13 employing the M13 sequence from the Ca^{2+} sensor YC3.6[16] and the calmodulin sequence from GCaMP6f[17] (**Fig. 1a-c**). We reasoned that inserting the CaM-M13 domain between Q88 and G89 would allosterically control enzymatic activity by modulating the structural integrity of the native disulfide bond (C65–C77) which stabilizes the rigid α4–α7 helical core of sbGLuc (**Fig. S1 and S2**). In the absence of Ca^{2+}, the inserted calmodulin domain destabilizes this interaction, whereas Ca^{2+} binding promotes reassembly of the split halves and restoration of luciferase activity. We called this split sbGLuc based Ca^{2+} indicator Lumicampsin or LMC, and LMC4 as this was the fourth split sbGLuc construct we generated.

To expand on LMC4, we engineered four additional variants: LMC5, LMC6, LMC7, and LMC8. LMC5 and LMC6 incorporate calmodulin sequences from the fluorescent calcium indicators GCaMP6s and GCaMP6m, respectively[17]. LMC7 and LMC8 incorporate calmodulin domains derived from the Ca^{2+}-dependent luciferases Ca^{2+}-NL and Ca^{2+}-eNL[16,18]. We selected the calmodulin domains based on their performance in either fluorescent Ca^{2+} indicators or prior

luciferase-based calcium sensors, with the goal of improving the dynamic range of our LMC variants (refer to **Fig. S3** for the amino acid differences across variants).

As the goal of LMC is to serve as a genetically encoded light source for activating blue light-sensing photoreceptors, we first confirmed its light emission spectra and Ca^{2+} responsiveness in cells across variants. HeLa cells were transfected with each LMC variant, incubated with 5 μM luciferin (CTZ), and stimulated with histamine to induce a physiologically relevant increase in intracellular Ca^{2+}. All variants retained a peak emission at roughly 490 nm (**Fig. 1d).** The percent change in light emission before and after histamine addition ranged from 232% to 288% across LMC variants. All LMC variants provide a blue-shifted optical report of intracellular calcium, enabling potential coupling to blue light sensitive optogenetic proteins required for the BLADe platform. Overall, there was no significant difference between the variants when compared to LMC4 (**Fig. 1e**).

Experiments in HeLa cells confirmed that LMC4 responds to histamine-induced Ca^{2+} release at physiologic levels, but this system does not allow experimental control of intracellular Ca^{2+} levels in living cells. To address this, we transfected HEK293 cells with LMC4 and applied ionomycin under defined extracellular Ca^{2+} concentrations ranging from 0.4875 μM to 39 μM (**Fig. 1f**). LMC4 reported ionomycin-induced Ca^{2+} flux at all tested concentrations. The decrease in bioluminescent signal at lower extracellular Ca^{2+} conditions (0.4785μM -1μM) reflects the loss of intracellular Ca^{2+} as ionomycin moves Ca^{2+} from high (intracellular) to low (extracellular) concentrations. We compared the response to 39 μM extracellular Ca^{2+} between HEK293 cells expressing LMC4 or GCaMP6f. Under the same conditions, LMC4 reported a 43% change in signal from baseline whereas GCaMP6f reported an 8.2% change, indicating a high dynamic range of calcium dependent light emission by LMC4 (**Fig. 1g**).

Having established that LMC4 responds to flux in intracellular Ca^{2+} levels in populations of cells, we next tested how subcellular localization affects its performance. We generated four LMC4 variants targeted to distinct subcellular compartments by adding varying localization sequences (**Fig. S4a**). As one of the intended uses of LMC4 is to activate light sensing proteins, we compared two ways of localizing the Ca^{2+}dependent light emitter to the inner cell membrane. We did this by adding either a C-terminal farnesylation (LMC4f) or an N-terminal myristoylation (myLMC4) signal. We compared Ca^{2+} induced light emission of the two constructs in HeLa cells and found the farnesylated version to perform significantly better (**Fig. S4b**). We compared LMC4f to LMC4er that localizes to the ER via a C-terminal KDEL sequence. HEK293 cells expressing either construct were tested in the absence (0 μM) or presence (39 μM) of extracellular Ca^{2+} and 10 μM CTZ. Acute Ca^{2+} flux was elicited by addition of 2 μM ionomycin. In the absence of extracellular Ca^{2+} the signal from LMC4er expressing cells was higher than that from LMC4f expressing cells due to ER mobilization of internal Ca^{2+} stores. In contrast, in 39 μM extracellular Ca^{2+} a high bioluminescence signal was observed in LMC4f expressing HEK cells with very low signal from LMC4er expressing cells (**Fig. S4c**). Lastly, we generated miLMC4 that targets the Ca^{2+} sensor to mitochondrial membranes. Mitochondria localization was confirmed by co-expressing miLMC4 with a mitochondrial tag BacMam2.0-Mito-GFP in HeLa cells. Confocal images show that the Mito-GFP tag and miLMC4 co-localize (**Fig. S4d**). Thus, we proceeded with LMC4f for all subsequent experiments, designated henceforth as LMC.

To test the ability of LMC to report Ca^{2+} dynamics in culture, we transfected primary cardiomyocytes with LMC and imaged them on DIV4 using an EMCCD camera. Cells were pre-incubated with luciferin (100 μM CTZ) for ~10 min before imaging. Addition of 10 μM ATP increased contractility and induced rapid Ca^{2+} transients with robust peaks (**Fig. 2a and b**). To

assess Ca^{2+} reporting in deep tissue, we transduced the hearts of Swiss Webster mice with AAV2/9-CAG-LMC4 and performed *in vivo* imaging three weeks later. Following intraperitoneal injection of 100 µg water-soluble luciferin, bioluminescent signals from the heart became visible through the chest within 10 minutes, peaked around 15 minutes post-injection, and gradually declined to baseline over the next hour (**Fig S5**).

Next, to test whether LMC could report neurotransmitter-evoked Ca^{2+} influx in neurons, we transfected primary hippocampal cultures and perfused luciferin (CTZ) followed by luciferin with glutamate. Bioluminescent signals were low with luciferin alone but increased after glutamate application **(Fig. 2c**). Time-locked traces showed a clear rise in bioluminescence following glutamate onset (**Fig. 2d**). Across individual neurons, we observed an increase in normalized peak responses with glutamate compared to luciferin alone (**Fig. 2e**). In addition, responses also exhibited high contrast relative to baseline, with a median fold-change of ~2–4 across neurons (**Fig. 2f**).

Having confirmed that LMC reports Ca^{2+} fluctuations in cardiomyocytes (*in vitro* and *in vivo*) and glutamate-evoked responses in hippocampal neurons, we next tested its performance in the brain *in vivo*. Mouse barrel cortex was injected in two distinct regions with AAV2/9-hSyn-LMC or calcium-insensitive GLuc and imaged through a cranial window in head-fixed mice. Luciferin (CTZ, 50 µL) was delivered into the lateral ventricle during continuous imaging, followed 5 min later by direct cortical NMDA injection (1 µL). Bioluminescence increased selectively in the LMC-expressing region after NMDA, whereas the calcium insensitive variant GLuc control region remained at baseline (**Fig. 2 g and h**). Together, these results validate LMC as a bioluminescent reporter of Ca^{2+} dynamics *in vitro* and *in vivo*. Further engineering of LMC is necessary for acquiring higher spatial and temporal resolution, as the image acquisition rate was restricted to ~1-4 Hz in our imaging conditions.

Bioluminescence as an activity-gated light source

We next compared LMC with other published bioluminescent Ca^{2+} indicators to evaluate its baseline emission and suitability as an activity-gated light source. HeLa cells were transiently transfected with LMC, BlueCaMBI[19], GLICO[20], or GeNL[18] and light emission was assayed in a luminometer following luciferin addition and histamine stimulation. Time-series traces show that BlueCaMBI, GLICO, and GeNL, produced higher overall photon output than LMC (**Fig. 3a**). Although these sensors were brighter, they also exhibited substantial baseline photon emission in the presence of luciferin under resting Ca^{2+} conditions, relative to their response after histamine stimulation. (**Fig. 3b**). All three indicators—BlueCaMBI, GLICO, and GeNL—have been reported to capture Ca^{2+} fluctuations, but in those studies, bioluminescence signal traces were typically normalized following luciferin pre-incubation[18–20]. While this normalization approach is appropriate for imaging relative Ca^{2+} dynamics, the high absolute photon emission at resting levels of Ca^{2+} limits their use as activity-gated light sources required for BLADe activation of photoreceptors.

High absolute brightness benefits imaging, but BLADe optogenetic applications require low basal emission and a large absolute increase in light output during Ca^{2+} influx. Consistent with this, when normalized to the luciferin baseline, only LMC exhibited a large relative change in photon emission following histamine-induced Ca^{2+} release (**Fig. 3c**). Accordingly, despite lower absolute brightness, the unique low background and high dynamic range of LMC positions it as an activity-gated light source ideally suited for converting intracellular signals into optical activation of downstream photoreceptors. At resting calcium levels, we hypothesize LMC light emission remains dim and is below the threshold needed to activate photoreceptor chromophores, minimizing spurious activation of light sensing proteins. We next asked whether this activity-dependent light source could drive optogenetic tools as the basis of the BLADe platform.

Integrating Ca^{2+} flux with change in transcription

LMC expressing cells showed low baseline bioluminescence in the presence of luciferin and a strong increase in light output following Ca^{2+} influx. We reasoned that LMC's activity-gated light emission could be used to photoactivate light-sensitive transcriptional effectors. To test this prediction, we co-expressed LMC with a light sensing transcription factor EL222[21]. In the presence of blue light, EL222 dimerizes and then binds to its promoter 5xC120, leading to transcription of the reporter gene (**Fig. 4a**). Next, we treated HeLa cells expressing each calcium sensor with luciferin for 15 minutes and measured the FLuc reporter 18 hours later in the following conditions: dark, luciferin-only, and luciferin + histamine (**Fig. 4b**).

All calcium dependent indicators produced FLuc transcription under luciferin treatment alone, indicating that transcription can be photoactivated even in the absence of calcium. In the presence of luciferin, baseline transcription was strongest for BlueCaMBI, GLICO, and GeNL, which were markedly brighter than LMC — a trend consistent with their higher baseline bioluminescence in luminometer traces (Fig. 3b). In contrast, only LMC showed a calcium-dependent increase in transcription, with a significant increase in FLuc signal in the luciferin + histamine condition compared to luciferin alone (**Fig. 4c**, LMC vs BlueCaMBI: P= 0.00998, GeNL: P=0.00609, GLICO: P=0. 00998, one sided Mann-Whitney U test). The overall transcriptional output from LMC remained modest compared to the other sensors, which is consistent with its lower total light output in luminometer assays (Fig. 3b). Having established that LMC produces calcium-dependent light sufficient to activate EL222 *in vitro*, we next tested whether the BLADe transcriptional system could function *in vivo*.

As a pilot study, we tested whether LMC could drive transcription in neurons *in vivo* when network activity was chemically elevated with NMDA. We performed stereotactic injections of AAV9-hSyn-LMC-P2A-dTomato, AAV9-CAG-EL222, and AAV9-5×C120-EYFP into the prefrontal cortex of anesthetized mice. After virus delivery, the craniotomy was immediately covered to further minimize unintended light exposure during recovery. After 2–3 weeks, to allow for maximal expression, mice received intraventricular injections of either NMDA + vehicle, luciferin (CTZ) alone, or luciferin + NMDA. These conditions allowed us to test: (1) non-specific background transcriptional activity in the absence of light (NMDA + vehicle), (2) light-dependent transcription in the context of spontaneous activity (luciferin alone), and (3) BLADe-mediated transcription (luciferin + NMDA).

Confocal imaging of tissue collected ~20 hours after treatment showed increased EYFP reporter labeling in individual LMC-expressing neurons from mice treated with luciferin + NMDA, compared to the other treatment groups (**Fig. 4d**). Single-cell analysis confirmed that EYFP reporter increase occurred across a range of dTomato expression levels (**Fig. 4e**), indicating that the Ca^{2+}-dependent enhancement of transcription was not due to differences in viral expression of LMC. Quantification of EYFP reporter/dTomato tool expression ratios revealed higher reporter expression in the luciferin + NMDA group compared to both the luciferin-only group and the NMDA-only group (**Fig. 4f**, Wilcoxon rank-sum test, Bonferroni-corrected luciferin+NMDA vs luciferin: P= 1.62 × 10^{-7}; luciferin+NMDA vs NMDA: P= 0.0057; luciferin vs NMDA: P = 0.196; pooled from FOVs of 197-350 cells/N=2 mice for each treatment group). The luciferin-only and NMDA-only groups were not significantly different from each other suggesting that reporter activation requires both intracellular calcium and bioluminescent light, consistent with LMC-BLADe gating. Together, these findings show that BLADe can function *in vivo* in the mouse brain to drive calcium-dependent transcription, but the overall magnitude of reporter labeling remains modest. Increasing light output of the Ca^{2+} dependent luciferase or improving the contrast

between active and inactive cells may help optimize this system for robust transcriptional labeling in future applications.

Integrating Ca^{2+} flux with change in membrane potential

To demonstrate the modularity of the BLADe platform, we tested whether LMC could drive light-sensitive ion channels. Following an action potential, the rapid influx of intracellular Ca^{2+} provides a convenient and high-resolution proxy for BLADe neural activation. We reasoned that LMC could detect these calcium transients and, through co-expression with an excitatory opsin, rapidly modulate membrane potential in an activity-dependent manner. To this end, we applied step current injections to hippocampal neurons *in vitro* in the presence of synaptic blockers to isolate cell-intrinsic responses. We then performed whole-cell patch-clamp recordings on neurons co-transformed with LMC and an opsin (**Fig. 5a**). By visualizing co-localized expression of an opsin-EYFP (green; here ChR2(C128S)) and the Ca^{2+}-dependent luciferase LMC-P2A-dTomato (red), we selected these double-positive neurons for testing the integration of cellular states via BLADe opsin activation.

We predicted that LMC generates light directly in response to Ca^{2+} influx which occurs during spiking induced by depolarizing current injections. We reasoned that increasing levels of depolarizing current in the presence of the luciferin would produce enough bioluminescence to further photoactivate ChR2(C128S)[22] via a cell-autonomous, positive feedback optical loop. In line with our prediction, luciferin perfusion during the same depolarizing current elicited significantly more detected action potentials than during vehicle perfusions **(Fig 5b, ii and iii,** N=16 neurons, $P= 4.954x10^{-9}$, paired sample Wilcoxon signed rank tests), indicating a light-dependent, cell-autonomous control of membrane voltage potential. Our findings demonstrate LMC bioluminescence is sufficient to photoactivate the opsin, they do not directly confirm BLADe control of opsins.

To isolate the activity-dependent component—which is expected to change how spikes are generated over the course of the current stimulation—we calculated a spike count fractional difference by evaluating the temporal distribution of spikes within each 1-second depolarizing current across trials. We subtracted the number of spikes in the second half of the current from the number of spikes in the first half, then normalized by the total spike count of a given trial. A value of +1 indicates that all spikes occurred in the first half, a value of 0 reflects an even distribution across both halves, and a value of -1 indicates that all spikes occurred in the second half. Therefore, we can determine how LMC-driven opsin activation changes action potential generation over the course of depolarization.

For neurons co-expressing the excitatory opsin under luciferin perfusion, we observed a significant shift toward fraction-difference values in the presence of the luciferin **(Fig 5b iv**, N=16 neurons, Kolmogorov-Smirnov test, KS= 0.25, P= 0.01319). Neurons co-expressing LMC and ChR2(C128S) generated action potentials in the initial 500 ms but produced additional spikes in the latter half of the 1s depolarizing step in the presence of the luciferin. The observed shift in firing patterns supports the activity dependent nature of LMC light emission and BLADe control of opsins. We hypothesize that the observed effect arises from an intensifying positive feedback loop mechanism, whereby sustained calcium influx over the course of the depolarizing current promotes ongoing opsin activation and alters spike timing.

In contrast, neurons co-expressing LMC and ChR2(C128S) that received two sequential vehicle perfusions—rather than luciferin in the second perfusion—showed no changes in both the frequency and temporal shift of the firing rate distributions **(Fig 5c ii-iv,** N=14 neurons, P=0.3117, paired sample Wilcoxon signed rank test, Kolmogorov-Smirnov test, KS=0.0597, P= 0.999). This

result confirms that the observed bias in spike timing requires luciferin, and by extension, BLADe's stimulus-dependent bioluminescence. To further ensure these changes depend on a functional opsin rather than bioluminescence alone, we next tested a non-photoconductive ChR2 mutant, ChR2(C128S)-E97R-D253A[23,24] ("DUD" opsin) alongside LMC (**Fig. S6**). There were no observed luciferin-induced shifts in spike timing or firing rate, confirming that BLADe control does not alter the excitability in the absence of an active light-sensitive channel.

Building on our findings with the excitatory opsin, we next tested whether BLADe could suppress firing in neurons expressing an inhibitory opsin. The same cell-autonomous bioluminescent positive feedback loop is expected to drive hyperpolarization rather than depolarization, leading us to predict a reduction in firing rate and spike timing. In line with our prediction, neurons co-expressing hGtACR2[25] and LMC exhibited fewer total spikes (**Fig. 5d, ii and iii,** N=16 neurons**,** *P*=0.3117*,* paired sample Wilcoxon signed rank test) and had decreased spikes in the second half of the depolarizing current (**Fig. 5d, iv,** N=16 neurons, Kolmogorov-Smirnov test, KS= 0.3888, *P*= 0.00809).

By coupling a depolarizing current and the resulting Ca^{2+} influx to opsin activation, BLADe provides an all-molecular strategy to sense and modulate neuronal excitability. This can be further customized based on the biophysical characteristics of the co-expressed opsin. Therefore, LMC integrates intracellular states to bidirectionally alter the magnitude and spiking dynamics in a cell-autonomous manner.

Moving beyond single-cell recordings, we next tested how LMC modulates firing rates at the network level by performing extracellular recordings on cultured cortical neurons plated on multi-electrode arrays (MEA)[26]. As in our patch experiment, we virally co-transduced an excitatory opsin ChR2(C128S)-EYFP and the Ca^{2+}-dependent luciferase LMC-P2A-dTomato (**Fig. 6a,b**). Time-locked multi-unit activity (MUA) traces revealed rapid population-level activity following luciferin or vehicle application (**Fig. 6c**). While vehicle addition alone can transiently increase network activity in MEA—likely due to mechanical or ionic effects of media perfusion—these responses were brief and stereotyped across independent experiments. To enable comparison, we aligned all trials to the application artifact, allowing time-locked analysis between vehicle and luciferin treatments. In doing so, we could distinguish true activity-dependent changes from non-specific network effects caused by vehicle addition. Vehicle and luciferin treatments were randomized on the same MEA culture. All comparisons used the same electrode sites with recording ~4-5 hours apart.

In the presence of luciferin, MUA was enhanced relative to vehicle one second after application (**Fig. 6d**)**.** Burst firing rates were similar between conditions (**Fig. 6e**), yet burst duration was significantly longer with luciferin (**Fig. 6f**). With burst firing rates unchanged but MUA elevated, we next tested whether neural activity was prolonged over time due to co-expression of an excitatory opsin with LMC. To this end, we analyzed the early phase as defined by the 0–50 ms window beginning immediately after the application artifact, corresponding to the initial rise in MUA relative to baseline (**Fig. 6g**). The time-locked window allowed for reliable comparisons of immediate firing between treatment conditions. The late phase was defined as the remaining portion of the 1-second window, from 100–1000 ms post-application, allowing us to test whether LMC modulates both the onset and sustained components of network activity.

Early phase firing rates were similar between vehicle and luciferin conditions indicating that initial responses to perfusion were comparable across treatments (**Fig. 6h**). Thus, the observed effects are not due to media-driven excitability or non-specific stimulation. In contrast, the late-phase response was significantly enhanced in the presence of luciferin (**Fig. 6i).** When normalizing the

354 late-phase MUA to the early-phase, we observed a clear enhancement in MUA consistent with
355 LMC activation with luciferin (**Fig. 6j**). The observed sustained effect on network excitability in the
356 presence of the luciferin suggests that LMC-driven light production prolongs neuronal activity via
357 local activation of the co-expressed excitatory opsin.
358
359 Lastly, we tested whether LMC could bidirectionally modulate firing rates in populations of cultured
360 neurons. In agreement with our whole-cell patch-clamp recordings, we observed a reduction in
361 MUA activity when LMC was co-transduced with the inhibitory opsin hGtACR2 (**Fig. S7**). To test
362 whether the observed inhibition requires LMC bioluminescence, we compared firing rate changes
363 before and after luciferin application in neurons expressing hGtACR2 alone (**Fig. S7, S8**) versus
364 those co-expressing LMC. Neurons lacking LMC showed a modest increase in activity (median
365 ΔFR = +7 Hz, n = 19), while LMC4-expressing neurons exhibited a strong suppression (median
366 ΔFR = –14 Hz, n = 51). The difference in MUA was significant (Wilcoxon rank-sum test, $P = 1.576$
367 $\times 10^{-10}$), confirming that luciferin-induced inhibition is specific to neurons expressing LMC.
368
369 Building on our *in vitro* electrophysiology observations, we next wanted to determine if LMC could
370 integrate physiological sensory inputs to alter neocortical networks. To move from cellular
371 responses and into tissue-level dynamics, we leveraged the well-characterized vibrissae circuit
372 to ask whether LMC can detect organism-scale sensory cues and reshape how they are encoded
373 within the neocortex. To this end, we injected Cre-dependent versions of LMC and the excitatory
374 opsin CheRiff[27] into the left cortex of Emx1-Cre mice to target both constructs to excitatory
375 pyramidal neurons within the vibrissa region of primary somatosensory cortex (vSI). Three to four
376 weeks later, we then performed extracellular recordings with laminar silicon probes in vSI. During
377 recordings in head fixed anesthetized mice, we constantly perfused ACSF or ACSF containing
378 luciferin (CTZ) over the cortical surface while delivering vibrissal deflections (**Fig. 7a, b**).
379
380 We first tested whether spontaneous neural activity driven bioluminescence could alone modulate
381 cortical activity via BLADe opsin activation. By expressing CheRiff in vSI pyramidal neurons, we
382 predicted increased MUA either through external LED stimulation or via activity-driven
383 bioluminescence. Consistent with our prediction, we observed increased spontaneous MUA in
384 the presence of luciferin relative to vehicle epochs (**Fig. 7c**, Wilcoxon signed rank test $p=2.32 \times$
385 10^{-10}, $p < 0.05$ with post hoc Bonferroni correction for multiple comparison, vehicle epoch: M=
386 26.4, SD= 16.61, median= 22.1, range= 5.4-80.4, CTZ epoch: M= 52.7, SD= 26.0, median= 43.6,
387 range= 17.5-126.6). These results suggest that LMC detects spontaneous intracellular calcium
388 transients and converts them into bioluminescent output sufficient to activate opsins and enhance
389 cortical spiking.
390
391 To confirm that the luciferin mediated enhancement was through opsin activation, we delivered a
392 brief sinusoidal LED stimulation (8 Hz sinusoidal pattern, 500 ms) at the end of each session.
393 Light responsive channels were observed relative to baseline spontaneous activity (**Fig. 7d**,
394 Kruskal-Wallis test $p= 3.23 \times 10^{-08}$; $p < 0.05$ with post hoc Bonferroni correction for multiple
395 comparison, during baseline: M= 24.13 Hz, SD= 8.51, median= 22.7, range: 14.4-54.8, during
396 stimulation: M= 83.1 Hz, SD= 96.63, median= 45.2, range=16.9-406.83). In contrast, non-
397 responsive channels had no change during LED stimulation (**Fig. 7d,** Kruskal-Wallis test $p > 0.05$,
398 during baseline: M=40.5, SD= 32.4, median= 22.7, range=0.1-173.26, during stimulation: 0.1-
399 173.07). Together with our luciferin epoch data, these results support that LMC increases
400 spontaneous cortical activity through bioluminescent optogenetic activation of CheRiff.
401
402 Following our observation that LMC enhances spontaneous cortical activity *in vivo*, we next tested
403 whether LMC can also rapidly amplify neural responses to external sensory inputs. To this end,
404 we tested for relationships between enhanced neural activity and vibrissae stimulus amplitude by

comparing MUA between vehicle and CTZ epochs. We delivered 10 vibrissae deflections at 20 Hz over a 500 ms stimulus window, with deflections randomized in amplitude. We observed evoked spikes within ~10–20 ms in vSI following low-amplitude vibrissae deflections, consistent with known sensory latencies in vSI and validating our electrode placement (**Fig. 7e**). There is an increase in MUA in sensory responsive channels in low stimulus trials in the presence of luciferin compared to vehicle (blue vs grey trace, **Fig. 7e**).

To isolate BLADe recruitment of cortical activity, we quantified evoked MUA in two non-overlapping post-stimulus windows: an early phase (0–25 ms), corresponding to the immediate sensory response, and a late phase (26–50 ms), where delayed or prolonged firing may reflect enhanced excitability. During the early response window (0–25 ms), which corresponds to direct thalamocortical input, firing rates were increased during the luciferin trials compared to vehicle (**Fig. 7f**, Kruskal-Wallis test, low: $p= 7.62 \times 10^{-06}$, mid: $p= 1.9 \times 10^{-06}$, max: $p= 3.72 \times 10^{-09}$, $p < 0.05$ with post hoc Bonferroni correction for multiple comparison). In the late window (26–50 ms), likely reflecting recurrent or sustained neocortical activity, we also observed enhancement in the presence of luciferin (**Fig. 7g,** Kruskal-Wallis test, low: $p= 7.63 \times 10^{-06}$, mid: $p= 3.81 \times 10^{-06}$, max: $p= 2.61 \times 10^{-08}$, $p < 0.05$ with post hoc Bonferroni correction for multiple comparison). We interpret this as evidence that LMC contributes to feedforward amplification of thalamocortical sensory inputs and delayed phases of cortical activity, likely driven by recurrent excitatory input through BLADe opsin activation. Collectively, these findings demonstrate that LMC enables cell-autonomous, activity-gated control of spontaneous and sensory evoked neocortical network dynamics *in vivo*. Through co-expression of LMC with light sensitive ion channels, BLADe photoactivation offers a genetically encoded strategy for sensing and manipulating neural dynamics.

Discussion

By using the concept of a luciferase split by a sensing moiety, any bioluminescent sensor can be made into an integrator by combining it with a photoreceptor. As a proof-of-concept and to demonstrate the versatility of the approach, we engineered a Ca^{2+} dependent luciferase and tested its ability to activate either a transcription factor or channelrhodopsins. We split the *Gaussia* luciferase variant sbGLuc and inserted a Ca^{2+} sensing moiety between the luciferase fragments. The engineered luciferase, called lumicampsin (LMC), contains a calcium sensing domain composed of the M13 peptide from YC3.6 and calmodulin from GCaMP6f. We identified critical design constraints for enabling activity dependent control of photosensing molecules: at resting intracellular Ca^{2+} levels, the presence of luciferin should generate minimal light output – ideally below the activation threshold of photoreceptor chromophores. Furthermore, elevation of intracellular Ca^{2+} must produce a sufficient increase in bioluminescence to cross this threshold and initiate photoreceptor activation. We successfully applied LMC to convert neural activity into transcription of a reporter gene and into changes in membrane potential *in vitro* and *in vivo*.

Several bioluminescent Ca^{2+} sensors have been developed by splitting luciferase enzymes and inserting Ca^{2+} sensing moieties[16,18–20,28,29]. Because bioluminescent probes have historically been far dimmer than fluorescent probes, most efforts have focused on maximizing light output. As a result, existing bioluminescent Ca^{2+} sensors successfully report Ca^{2+} fluctuations, but with Ca^{2+} dependent increases in signal riding on top of high baseline light emission. For many imaging applications, baseline bioluminescent signal in the absence of high Ca^{2+} is acceptable. However, this is incompatible with the BLADe approach, as the background light emission by itself is already high enough to activate a photoreceptor. To avoid unintended photoactivation, the split luciferase must produce very low levels of light emission at rest –when luciferin is present but intracellular calcium is low. Under these conditions, the luciferase enzyme should remain incompletely

456 reconstituted and emit minimal light. Only upon calcium binding—or the presence of a specific
457 co-factor needed for enzyme reconstitution—should bioluminescence steeply increase to a level
458 sufficient for activating nearby photoreceptors. Comparison to other bioluminescent Ca^{2+} sensors
459 revealed this critical difference in SNR for the LMC construct used here to establish the BLADe
460 paradigm. This also motivated the development of a much brighter Ca^{2+} dependent luciferase,
461 CaBLAM, that fulfills these criteria and will enable improved performance of BLADe-based
462 systems[30].
463
464 There is an increasing need to not only monitor biochemical fluctuations in real time, but to
465 permanently mark and modify cells based on intracellular activity, enabling their subsequent
466 identification and targeted manipulation. The drive for developing such integrators has been most
467 prolific in neuroscience, challenged by the question of how to identify and study the ensemble of
468 active neurons underlying a specific behavior: Which cells in which contexts form the necessary
469 chain of actors that selectively lead to perceptions, actions and cognition. A recent generation of
470 approaches was created that attempts to advance this area of study by using calcium sensitivity
471 and engineered TEV protease as the mechanism that creates activation-dependence[31–33]. The
472 leading examples of this approach, Cal-Light[31] and FLARE[32], employ timed light to target specific
473 behavioral epochs. In essence, the coincidence of light and neural activity results in release of a
474 transcription factor: light application leads a LOV domain to expose a protease cleavage site; the
475 protease will only be in proximity to the cleavage site in the presence of high Ca^{2+}, with
476 photostimulation providing a high degree of temporal and spatial control. This Ca^{2+} dependent
477 protease strategy has significant limitations in that it requires a fairly complicated molecular
478 design, increasing the potential for failure points in distinct cell types. More importantly, light
479 pulses from a fiber optic are required to drive expression, which does not allow whole ensemble
480 tagging across the brain. In contrast, BLADe relies on the straightforward design of a split
481 luciferase that reconstitutes with increasing levels of Ca^{2+} and emits light sufficient for activating
482 light-sensing transcription factors in the presence of luciferin, as demonstrated *in vivo* by
483 expression of fluorescent reporters in mouse neocortex. As the system is chemically gated,
484 systemic application of the luciferin will reach each cell expressing BLADe integrators based on
485 increasingly improved bioavailability of luciferins.
486
487 One of the most powerful applications of BLADe for molecular integration is as a tool for all-
488 molecular, real-time feedback regulation. The lives of cells, organs and organisms are dependent
489 on chemical fluctuations on the time scale of milliseconds to seconds. Failure to regulate these
490 ongoing dynamics is a common motif in disease. When the proper feedback control of a local
491 augmenting process fails, runaway activity can result—as observed in activity-dependent cell
492 death and spreading neural activity during a seizure. Conversely, failure to amplify local
493 fluctuations can devastate biological processes such as glucose-driven insulin production or
494 information processing in the brain. When paired with ion-moving optogenetic actuators, BLADe
495 enables the conversion of neural activity into real-time changes in membrane potential, supporting
496 closed-loop feedback control of neuronal activity. The efficacy of this self-regulation was
497 demonstrated *in vivo* where LMC converted spontaneous activity and sensory evoked responses
498 into activity dependent control of neocortical network dynamics.
499
500 Recently, bioluminescence emitted from an intact luciferase has been applied to couple a sensor
501 for neuronal hyperactivity with a molecular actuator capable of switching off neuronal activity in
502 an all-molecular negative feedback loop at the single neuron level[34]. When excited at ~400–410
503 nm, the ratiometric pH sensor E2GFP increases light emission at 510 nm in proportion to
504 acidification—a hallmark of neuronal hyperactivity in seizures. To generate a pH sensitive
505 inhibitory luminopsin (pHIL), three proteins were fused together: a hyperpolarizing opsin
506 (eNpHR3,0), E2GFP, and a *Renilla* luciferase. The N-terminus of the construct contained the

eNpH3.0, a chloride pump activated by 510 nm light. E2GFP was placed in the center, serving as the pH-responsive optical relay for amplifying bioluminescence. The C-terminus of the E2GFP was fused to the *Renilla* luciferase variant RLuc8, which emits at 405 nm when supplied with bisdeoxycoelenterazine (CTZ 400a). Through a two-step resonant energy transfer cascade triggered by acidification in the presence of luciferin, pHIL translates the hyperactivity-induced intracellular acidosis into silencing of neuronal activity. This was demonstrated *in vivo* by mitigating acute tonic-clonic seizures induced by pilocarpine and by counteracting audiogenic seizures in the PRoline-Rich Transmembrane protein 2 knockout (PRRT2 KO) mouse, a model of genetic epilepsy. While pHIL is designed to specifically convert neuronal hyperactivity into silencing, BLADe includes and transcends this application of real-time feedback. Co-expression of the BLADe LMC integrator with an inhibitory or excitatory opsin resulted in neural activity-driven hyperpolarization or additional depolarization, respectively, of the individual cell and neural networks.

The development of tools for all-molecular real-time feedback regulation in neuroscience is motivated by the desire to replace problematic “externally closed-loop” systems by “internal closed-loop sensor-actuators” working at the level of individual neurons. Current solutions are based on implanted hardware and computer-based detection algorithms to conduct detection and deliver control. For example, in neuroscience approaches to real-time detection and feedback control for altering maladaptive activity patterns such as overly exuberant neural bursting rely on signals being tracked using electrodes, and patterns detected by computer algorithms that trigger countermanding stimulation through implanted electrodes or fiber optics for electrical or optogenetic regulation[35,36]. This strategy has shown success, for example in stopping epileptic seizures dependent on thalamic bursting with optogenetic drive[37]. These closed-loop approaches for dynamic brain regulation are promising but have key limitations. These methods require chronic implants to detect patterns and deliver stimuli, and electrical stimuli or injected chemicals impact all adjacent cells. An ideal strategy would not require implants, would only regulate cells when they express maladaptive patterns, and would specifically regulate only those cells exhibiting aberrant patterns, not the entire field of cells near an electrode.

The BL-ADe platform provides a solution to dynamic control, detecting calcium increases to drive feedback through local opsins with cellular precision. By providing real-time feedback control, driving opsins only when a cell is active, it is a unique way to sense such dynamics and locally and immediately alter their trajectory within a single neuron. This control mechanism can enhance behaviorally relevant neural activity patterns (e.g., sensory responses), but only when the cells are activated above a threshold. This method can allow triggering based on underlying dynamics in specific cell types in specific foci, for example, briefly increasing the firing of only those pyramidal neurons that burst, to test if their increased firing duration enhanced sensory detection. This approach is also ideal for directly targeting dynamical processes. As an example, using BLADe to trigger enhanced hyperpolarization (or, depolarization) only after individual neurons show a large calcium event is ideal for altering the operative mechanism to extend or suppress macro-scale phenomena within tissue.

Here we developed a highly versatile Bioluminescent Activity Dependent (BLADe) platform for converting intracellular activity to photoreceptor activation. As proof-of-principle, our data show that a Ca^{2+} dependent luciferase can integrate Ca^{2+} fluctuations to drive transcription and change membrane potential. The BLADe platform can be furthered by engineering Ca^{2+} dependent luciferases with higher light emission, faster kinetics, and expanded dynamic ranges for Ca^{2+} sensing. Beyond these proof-of-principle applications, Ca^{2+} signals are ubiquitous in biology and essential for life, driving, for example, contraction in muscles and insulin release in pancreatic cells, in addition to information processing in neurons. Importantly, the modularity of the BLADe

558 framework allows Ca^{2+}-dependent light activation to be coupled to a wide range of light-sensing
559 actuators, providing experimental control over diverse molecular outcomes depending on the
560 user's goal. Moreover, the luciferase can be split by different sensing domains, providing a
561 general mechanism for cells to detect their own biochemical state and then drive discrete user-
562 defined outcomes. Further developed and improved versions of these tools are expected to have
563 broad applications. In basic research, this paradigm allows investigators to selectively detect, and
564 then suppress or amplify, specific biological events, a unique approach to understanding the role
565 of those processes. In potential therapeutic applications it allows sensing and discontinuing
566 aberrant activity before it can cause harm, or stopping pathological processes from continuing, or
567 amplifying and rescuing failing processes, without the use of implanted devices and regulated by
568 simple peripheral injection of a luciferin.
569
570
571 **MATERIALS AND METHODS**
572
573 **Chemicals**
574 Coelenterazine (CTZ) for in vitro (#303) and in vivo (#3031) experiments was purchased from
575 Nanolight Technologies. The Calcium Calibration Buffer Kit #1 from Life Technologies was used
576 to prepare Zero Ca^{2+} buffer and 39 μM Ca^{2+} buffer. All other chemicals, including Ionomycin and
577 Histamine, were purchased from Sigma.
578
579 **Plasmids**
580 A pcDNA3.1 backbone with the CMV promoter was used to insert gBlocks (IDT) that encode for
581 N-sbGluc, CaM-M13 variants, C-sbGluc and p2a dTomato by Gibson cloning (New England
582 Biolabs HiFi DNA Master Mix). Coding sequences from plasmids for GCaMP6f, hGtACR2,
583 ChR2(C128S), and CheRiff (Addgene) and for BlueCaMBI and GLICO (synthesized by Genscript)
584 were cloned into the pcDNA3.1-CMV backbone. Expression plasmids for VP-EL222 and 5xC120-
585 FireflyLuc were kindly provided by Dr. Kevin Gardner, CUNY, New York, NY, and for GeNL(Ca2+)
586 by Dr. Takeharu Nagai (Addgene). For viral vectors, coding sequences were cloned into a pAAV
587 vector downstream of a CAG or hSyn promoter, or into a pAAV-Efla-DIO construct. For list of
588 plasmids used see Supplementary Table 1.
589
590 pcDNA3.1-CAG-VP-EL222 and pcDNA3.1-5xC120-FireflyLuc were kindly provided by Dr. Kevin
591 Gardner, CUNY, New York, NY
592 pAAV.Syn.GCaMP6f.WPRE.SV40 was a gift from Douglas Kim & GENIE Project (Addgene
593 plasmid # 100837 ; http://n2t.net/addgene:100837 ; RRID:Addgene_100837)
594 GeNL(Ca^{2+})_520/pcDNA3 was a gift from Takeharu Nagai (Addgene plasmid # 85204 ;
595 http://n2t.net/addgene:85204 ; RRID:Addgene_85204)
596 pLenti-CaMKIIa-hChR2(C128S)-EYFP-WPRE was a gift from Karl Deisseroth (Addgene plasmid
597 # 20294 ; http://n2t.net/addgene:20294 ; RRID:Addgene_20294)
598 pFUGW-hGtACR2-EYFP was a gift from John Spudich (Addgene plasmid # 67877 ;
599 http://n2t.net/addgene:67877 ; RRID:Addgene_67877)
600 pAAV-hSyn-CheRiff-eGFP was a gift from Adam Cohen (Addgene plasmid # 51697 ;
601 http://n2t.net/addgene:51697 ; RRID:Addgene_51697)
602
603 **AAV**
604 AAV2/9 preparations were generated by triple lipofection of HEK293-FT cells and harvesting viral
605 particles as previously described[5].
606
607
608

609 **Animals**
610 All experiments involving animals were carried out following the guidelines and protocols
611 approved by the Institutional Animal Care and Use Committee at the participating universities and
612 were in compliance with the US National Research Council's Guide for the Care and Use of
613 Laboratory Animals, the US Public Health Service's Policy on Humane Care and Use of
614 Laboratory Animals, and Guide for the Care and Use of Laboratory Animals. Mice were group-
615 housed in ventilated cages under 12-hour reverse light cycle, provided with tap water and
616 standard chow and allowed to feed ad libitum. C57/BL6 (JAX #000664), Emx1-Cre (JAX#
617 005628), and Swiss Webster (Charles River) mice of both sexes were used.
618
619 **Cell Culture and Cell Transformation**
620 HEK293 and HeLa cells were obtained from ATCC (American Type Culture Collection),
621 expanded, and aliquots at low passage numbers were frozen. Cells were grown in Gibco DMEM
622 media supplemented with 10% Fetal Bovine Serum, 1% Glutamax, 0.5 % Pen-Sterp, 1% Non-
623 Essential Amino Acids and 1% sodium pyruvate. Cells were cultured at 37ºC and 5% atmospheric
624 carbon dioxide. Cells were transfected with Lipofectamine 2000 or 3000 in accordance with the
625 manufacturer's instructions.
626
627 Primary E18 rat hippocampal neurons were prepared from tissue shipped from BrainBits
628 (Transnetyx) following the vendor's protocol. Neurons were grown in Gibco Neurobasal Media
629 supplemented with 2% B27 supplement and 0.1% gentamycin and 1% Glutamax. Neurons were
630 nucleofected with plasmids of interest using the Lonza 2b Nucleofector and Rat Neuron
631 Nucleofector Kit (Lonza, VPG-1003) according to the manufacturer's instruction, then seeded. Or
632 neurons were nucleofected, seeded, then transduced with AAV the next day. Neurons were
633 seeded on PDL-coated glass coverslip (Neuvitro) in 12-well tissue culture plates (1 x 10^5 neurons
634 per well) or were plated on the electrode area of 1-well MEA dishes (60MEA200/30iR-Ti; Multi
635 Channel Systems, Germany) coated with PEI (0.1%) and laminin (50µg/ml) (1x10^5 neurons/10
636 µL/well) as described in detail in Prakash 2020[26].
637
638 Primary cardiomyocytes were harvested from E18 Swiss Webster mice, papain digested and
639 plated on 35mm glass bottom dishes (MatTek) for real time bioluminescence imaging. Primary
640 cardiomyocytes were grown in Claycomb Media supplemented with 10% HL-1 screened FBS,
641 100µg/mL penicillin/streptomycin, 0.1mM norepinephrine and 2% Glutamax. Cells were
642 nucleofected with plasmids of interest using the Lonza 2b Nucleofector and Rat cardiomyocyte
643 Nucleofector Kit (Lonza, VAPE-1002) according to the manufacturer's instruction.
644
645 **Microscopy**
646 Initially, all transfected cells were imaged using a Zeiss Axio Observer A1 microscope with a LD
647 A-Plan 20x/0 air objective and a Hamamatsu Orca Flash 4.0 CMOS camera to confirm expression
648 by fluorescence microscopy at 50ms exposure except for LMCer, which was imaged at a 10
649 seconds exposure. Confirmation of subcellular localization and imaging of brain sections were
650 done on an Olympus Fluoview 300 CLSM confocal microscope with a 60x/1.3 Oil objective.
651
652 **Bioluminescence Imaging**
653 *In vitro*
654 For photon counting HEK293 and HeLa cells were seeded on Costar 96 well clear bottom white
655 plates and luminescence was measured in a SpectraMax® L luminometer (Molecular
656 DevicesTM). For real-time bioluminescence imaging we used a Zeiss Axio Observer A1
657 microscope with a Fluar 40x/1.3 Oil objective with either a Hamamatsu Orca Flash 4.0 CMOS
658 camera or an Andor iXon Ultra 888 EM-CCD camera with their respective softwares. HEK293
659 and HeLa cells were imaged in imaging solution (CaCl2 1.25mM, HEPES 19.7mM, KCl 4.7mM,

660 KH2PO4 1.2mM, MgSO4 1mM, NaCl 130mM, dextrose 0.5, pH 7.2-7.4) with either 100μM or 12.5
661 μM CTZ. Primary cardiomyocytes were imaged in Tyrode's solution (NaCl 137mM, KCl 2.7mM,
662 MgCl2 1mM, CaCl2 1.8mM, Na2HPO4 0.2mM, NaHCO3 12mM, D-glucose 5.5mM, pH 7.2-7.4)
663 supplemented with 10μM norepinephrine and 100 μM CTZ.
664
665 *In vivo*
666 Brain: AAV2/9-hSyn-LMC4f-P2A-dTomato (450 nl) was injected across three locations in left
667 primary somatosensory (SI) cortex (150 nl per site) as described in detail in Gomez-Ramirez
668 2020[38]. Water-soluble CTZ (Nanolight Technology #3031) was diluted to yield a concentration of
669 2.36 mM. CTZ and NMDA injections were done directly in cortex. Bioluminescence was measured
670 using an electron multiplier charge coupled device (EMCCD) camera (Ixon 888, Andor) attached
671 to a Navitar Zoom 6000 lens system (Navitar, 0.5× lens). Images were collected in a custom-
672 made light-tight chamber with an exposure time of 10 s, and the EM gain set to 30. Imaging data
673 were recorded using the Solis image acquisition and analysis software (Solis 4.29, Andor).
674
675 **Electrophysiology recordings from primary neurons**
676 Neurons (rat E18, cortical) were co-nucleofected with LMC4f and either an inhibitory opsin,
677 hGtACR2, an excitatory opsin, ChR2(C128S), or a "Dud" opsin, ChR2(C128S)-E97R-D253A.
678 Post nucleofection, neurons were plated on laminin-coated glass coverslips (15mm, Neuvitro) in
679 culture medium consisting of Neurobasal Medium (Gibco # 21103-049), B-27 supplement (Gibco
680 # 17504-044), 2 mM Glutamax (Gibco # 35050-061), and 5% Fetal Calf Serum (FCS). The
681 following day, the medium was replaced with serum-free medium (NB-Plain medium). Half of the
682 medium was replaced with fresh NB-Plain medium every 3–4 days thereafter. Neurons were used
683 for whole cell patch clamp recordings between DIVs 21–25. For patch clamp recording, a
684 coverslip was transferred to a recording chamber mounted on an upright microscope (BX51WI,
685 Olympus) and perfused with aCSF containing (in mM): 121 NaCl, 2.8 KCl, 1 NaH_2PO_4, 26
686 $NaHCO_3$, 2 $CaCl_2$, 2 $MgCl_2$ and 15 D-glucose (310 mOsm/kg, pH 7.3-7.4) at a rate of 1.5 ml/min.
687 All solutions were bubbled with a gas mixture of 95% O_2 and 5% CO_2. Whole-cell patch clamp
688 recordings were performed using a Multiclamp 700b amplifier and Digidata 1440 digitizer together
689 with the pClamp recording software (Molecular Devices). Borosilicate glass micropipettes were
690 manufactured using a PC-100 puller (Narishige) and had resistances of 3–5 MΩ. In current clamp
691 recordings, pipettes were filled with intracellular solution containing (in mM): 130 K-gluconate, 10
692 KCl, 15 HEPES, 5 Na_2-phosphocreatine, 4 Mg-ATP and 0.3 Na-GTP (310 mOsm/kg, pH 7.3).
693 The aCSF was supplemented with D-AP5 (50 μM), CNQX (15 μM) and picrotoxin (100 μM) to
694 block fast glutamatergic and GABAergic synaptic transmission. Rs was compensated by using
695 bridge balance. Firing frequencies were calculated from the total number of action potentials
696 produced per unit time during depolarizing current injections (10 sweeps, 1.5 sec duration) in
697 episodic stimulation acquisition mode, at a membrane potential of -70mV, before and after CTZ
698 (100 μM) or vehicle treatments.
699
700 **MEA Recordings**
701 Once the neurons were matured (DIV14-DIV19), only those were included in the analysis that
702 were consistently spiking and were positive for expression of their respective opsins as tested by
703 shining blue LED light (470nm) on the culture and recording increase or decrease of spiking. Total
704 recording time was 900 seconds. MEAs were subjected to 10μM CTZ at around 600 seconds.
705 Experimental cultures expressed both LMC4f and an opsin (ChR2(C128S) or hGtARC2), while
706 control MEAs only expressed the opsin. MC Rack software was used for data acquisition. All MEA
707 analysis was done offline with MC Rack software (MultiChannel Systems; RRID:SCR_014955)
708 and NeuroExplorer (RRID:SCR_001818) as described in detail in Prakash et al., 2020[26].
709
710

Transcription *in vitro*

HeLa cells were used to test whether LMC-driven light emission could activate transcription through the light-responsive transcription factor EL222. Cells were plated in 6-well plates and transfected at ~80–90% confluency using Lipofectamine 2000 (Thermo Fisher). Each well received a total of 2 µg DNA, composed of the following: 666 ng EL222 (light-sensitive transcription factor), 333 ng 5×C120-FLuc (EL222-responsive firefly luciferase reporter), and 1000 ng LMC4f-dTomato (calcium-dependent luciferase). Parallel wells were transfected with other calcium-dependent bioluminescent sensors (GeNL, GLICO, BlueCaMBI) and matched FLuc reporters.

Three hours after transfection, cells were trypsinized (300 µL trypsin per well) and replated into PDL-coated, white-walled, clear-bottom 96-well plates (~100,000 cells per well). Cells were allowed to adhere for 9–12 hours before stimulation. For transcriptional activation, 100 µL of stimulation buffer was added per well (1:1 with cell media) for a final well volume of 200 µL. The stimulation solution contained 100 µM CTZ or hCTZ (depending on the sensor), with or without 10 µM histamine. Vehicle controls received no treatment. After stimulation, cells were incubated for 7–9 hours before transcriptional reporter readout.

For FLuc transcriptional measurement, activity was recorded 18 hours after stimulation using a luminometer. Prior to measurement, cells were washed and incubated in phenol red–free media (100 µL per well). D-luciferin (final 150 µg/mL) was prepared from a frozen 60 mg/mL stock by serial dilution into Opti-MEM. For each well, 25 µL of 750 µg/mL D-luciferin working stock was injected into 100 µL of media. FLuc bioluminescence was recorded immediately after injection.

Transcription *in vivo*

To test bioluminescent dependent transcription *in vivo*, we co-injected three AAV constructs into the prefrontal cortex of anesthetized mice: AAV9-hSyn-LMC4f-P2A-dTomato (Ca^{2+}-sensitive luciferase), AAV9-CAG-EL222 (light-activated transcription factor), and AAV9-5×C120-EYFP (EL222-responsive reporter). Viral solutions were mixed prior to injection to a total volume of 1 µL per site, yielding final per-virus titers of: LMC4f (1×10^{10} GC), EL222 (0.7×10^{10} GC), and C120-EYFP (0.3×10^{10} GC). The injection was targeted to the left medial prefrontal cortex at +0.37 mm anterior to bregma, 3.0 mm lateral. Following injection, the craniotomy was sealed to minimize ambient light exposure during recovery.

After 7 days, mice received intraventricular (ICV) injections of one of three treatments: (1) NMDA + vehicle, (2) luciferin (CTZ) alone, or (3) luciferin + NMDA. These conditions were used to assess background transcription, spontaneous activity-driven transcription, and full BLADe-dependent transcriptional gating, respectively. Injections were performed using a 26-gauge needle and 10 µL Hamilton syringe, targeting the right lateral ventricle (AP: –0.5 mm, ML: –1.1 mm, DV: –2.0 mm from bregma). The luciferin was prepared fresh by dissolving coelenterazine (NanoLight #3031) in sterile water to a stock concentration of 1.6 mM, then when injected was assumed to be diluted 1:8 in CSF within the ventricle to yield a final injection concentration of 200 µM. NMDA was prepared at a working concentration of 75 ng/µL in sterile water. For combined delivery, 1 µL of NMDA solution (75 ng) was mixed with 4 µL of luciferin solution per injection (final 5 µL per mouse, injected over 5mins). Solutions were prepared under minimal light and protected from exposure throughout. After injection, mice were removed from the stereotaxic apparatus and allowed to recover. Brains were collected for histological analysis ~20 hours after ICV injection. Mice were anesthetized and transcardially perfused with PBS followed by 4% paraformaldehyde. Coronal brain sections were collected and imaged by confocal microscopy to quantify EYFP reporter expression.

To analyze calcium- and light-dependent transcriptional activation *in vivo*, we quantified EYFP reporter expression in dTomato-labeled neurons across experimental groups. Confocal images from all treatment conditions (NMDA-only, luciferin-only, luciferin + NMDA) were analyzed. First, dTomato+ images were pooled and segmented from maximum intensity projections using the MATLAB 'cell-segm' thresholding and size-filtering algorithm[39], ensuring unbiased detection across all fields of view. The resulting binary masks were then applied to the corresponding EYFP images to extract raw per-cell reporter fluorescence from each dTomato+ neuron. Finally, cells were grouped by treatment, and the ratio of EYFP to dTomato fluorescence was computed per cell to normalize for expression variability.

Electrophysiology *in vivo*

To express LMC and CheRiff in excitatory cortical neurons, we injected AAVs into the left virbissa primary somatosensory cortex (vSI) of Emx1-Cre mice (3–4 month old). AAV1-EF1a-DIO-LMC4f and AAV1-EF1a-DIO-CheRiff-EYFP were mixed 1:1 and delivered in a single injection (1 µL total) using a 33-gauge Nanofil syringe. Using a dental drill, a burr holes was made for AAV injection. The injection site was located 1.5 mm posterior and 3.0 mm lateral to bregma, and the needle was lowered to a depth of 500–1000 µm below the pial surface. Virus was infused at a rate of 50 nL/min over ~20 minutes. Following injection, the needle was held in place for 10 min, then raised to 200 µm and held for an additional 10 min before full withdrawal to allow the virus to spread across the layers of the cortex. During the same surgery, a custom metal headpost was implanted for head fixation. After exposing the skull, a thin layer of clear Metabond was applied to stabilize the surface while keeping bregma and surface vasculature visible. The headpost was then affixed using additional Metabond, positioned off-center to leave vSI accessible. The short arm was angled over the left ear to allow right-side whisker stimulation. After injection and headpost implantation, the craniotomy was covered with mineral oil and sealed with Metabond. Animals recovered for at least 3 weeks before recordings.

After 2–3 weeks of recovery, mice were anesthetized with isoflurane (1.2–1.4%) and head-fixed. The craniotomy used for AAV injection was reopened and expanded to 1 mm to expose the underlying cortex and target the same vSI region as the viral delivery. Throughout the procedure, the brain remained covered in carbogenated ACSF (95% O_2 / 5% CO_2) under constant perfusion. Animals were placed in a light-tight, electrically shielded chamber and maintained under anesthesia. Mice were secured in place to allow perfusion tubing to be positioned next to the craniotomy, allowing for constant aCSF inflow (for bioluminescence CTZ was diluted to 50 µM in aCSF). All macrovibrissae on the right side of the mouse were secured ~3mm from the mystacial pad. A custom-made clamp was glued to a piezoelectric bender (Noliac CMBP09), positioned to move all macrovibrissae in the caudorostral direction, with a half-sine wave velocity profile with a rising phase (6ms) and a slower relaxation phase (20ms). On each trial, 20Hz vibratory vibrissal stimulus trains (10 deflections, 500ms) were delivered for 1000 trials total. On a trial by trial and randomized basis, the stimulus amplitude varied between 0 to maximal amplitude (~1mm deflection). For each recording session, aCSF was constantly perfused for the first 500 trials and luciferin (CTZ) was then perfused for the remaining 500 trials.

All recordings in barrel cortex were conducted under light isoflurane anesthesia. Laminar probes consisted of single shank,32-channel silicon probes with a fiber optic 50µm above the highest recording site (A1x32 Poly2-5mm-50s-177-OA32LP, Neuronexus Technologies; 0.15mm silver wire reference). Data was sampled at 30kHz and passed through a digital amplifier (Cereplex-µ, Blackrock Microsystems), and directed through HDMI to the Cereplex Direct data acquisition box (Blackrock Microsystems). The 32-channel linear silicon probe was inserted perpendicularly into cortex using a micromanipulator at ~10 µm/s until the top contact of the electrode disappeared beneath the pial surface. The probe was allowed to settle for ~30–60 minutes before recording.

Luciferin (coelenterazine; NanoLight #3031) was freshly prepared in sterile water (1 µg/mL) and diluted into ACSF to a final concentration of 20 µM. Following an initial recording period under vehicle ACSF, the perfusion line was switched to CTZ-containing ACSF to enable continuous bath application during the second half of the session. Flow rate and volume were monitored to maintain complete coverage of the craniotomy and probe without overflow.

Raw electrophysiological data were downsampled to 10 kHz. For each recording, electrode contacts with RMS values exceeding three times the interquartile range above the 75th percentile or below the 25th percentile across the 32-channel array were flagged as noise and removed for further analysis. All remaining electrodes were re-referenced to the common average[40]. MUA was estimated by converting raw spike times into instantaneous firing rates using 1 ms bins. For luciferin experiments, stimulus-aligned firing rates were extracted from trials before and after the defined luciferin application time. Channels were classified as luciferin-responsive if the 99% confidence interval of the post-luciferin firing rate (bootstrapped, n = 1000) did not overlap with the baseline distribution. For sensory stimulation experiments, MUA peristimulus time histograms (PSTHs) were constructed by aligning spike data to stimulus onset and binning at 1 ms. PSTHs were smoothed using a Gaussian kernel (window = 20 ms, SD = 3 ms) and averaged across trials. PSTHs were computed separately for pre- and post-luciferin trial blocks.

Statistics

All analysis was carried out using MATLAB and SPSS software. Data are displayed as mean±standard error of the mean (SEM). We ran two-way repeated measures and One-way ANOVA. Tukey's post hoc was run where significant main effect was found.

Electrophysiological in vivo data was high pass filtered at 250Hz to extract spikes. Spike data was thresholded at -63µV and sorted for each channel based on waveform characteristics using Principal Components Analysis (PCA). Spikes were binned to calculate frequency of firing over time. Differences between groups were assessed using two-way repeated measures ANOVAs (repeat trials per mouse). For ex vivo electrophysiological data, statistical significance between groups was determined using Student's T-test.

REFERENCES

1. Love, A. C. & Prescher, J. A. Seeing (and Using) the Light: Recent Developments in Bioluminescence Technology. *Cell Chemical Biology* vol. 27 904–920 at https://doi.org/10.1016/j.chembiol.2020.07.022 (2020).
2. Rost, B. R., Schneider-Warme, F., Schmitz, D. & Hegemann, P. Optogenetic Tools for Subcellular Applications in Neuroscience. *Neuron* **96**, 572–603 (2017).
3. Losi, A., Gardner, K. H. & Moglich, A. Blue-Light Receptors for Optogenetics. *Chem. Rev.* **118**, 10659–10709 (2018).
4. Berglund, K., Birkner, E., Augustine, G. J. & Hochgeschwender, U. Light-Emitting Channelrhodopsins for Combined Optogenetic and Chemical-Genetic Control of Neurons. *PLoS One* **8**, e59759 (2013).
5. Berglund, K. *et al.* Luminopsins integrate opto- and chemogenetics by using physical and biological light sources for opsin activation. *Proc. Natl. Acad. Sci. U. S. A.* **113**, E358–E367 (2016).
6. Tung, J. K., Gutekunst, C.-A. & Gross, R. E. Inhibitory luminopsins: genetically-encoded bioluminescent opsins for versatile, scalable, and hardware-independent optogenetic inhibition. *Sci. Rep.* **5**, 14366 (2015).
7. Crespo, E. L., Bjorefeldt, A., Prakash, M. & Hochgeschwender, U. Bioluminescent Optogenetics 2.0: Harnessing Bioluminescence to Activate Photosensory Proteins In Vitro and In Vivo. *J. Vis. Exp.* (2021) doi:10.3791/62850.

863 8. Li, T. *et al.* A synthetic BRET-based optogenetic device for pulsatile transgene
864 expression enabling glucose homeostasis in mice. *Nat. Commun.* **12**, (2021).
865 9. Parag-Sharma, K. *et al.* Engineered BRET-Based Biologic Light Sources Enable
866 Spatiotemporal Control over Diverse Optogenetic Systems. *ACS Synth. Biol.* (2020)
867 doi:10.1021/acssynbio.9b00277.
868 10. Naim, N. *et al.* Luminescence-activated nucleotide cyclase regulates spatial and temporal
869 cAMP synthesis. *J. Biol. Chem.* (2019) doi:10.1074/jbc.AC118.004905.
870 11. Kim, E. H. *et al.* Self-luminescent photodynamic therapy using breast cancer targeted
871 proteins. *Sci. Adv.* **6**, (2020).
872 12. Shramova, E. I., Frolova, A. Y., Filimonova, V. P., Deyev, S. M. & Proshkina, G. M.
873 System for Self-excited Targeted Photodynamic Therapy Based on the Multimodal
874 Protein DARP-NanoLuc-SOPP3. *Acta Naturae* **15**, 100–110 (2023).
875 13. Yeh, H.-W. & Ai, H.-W. Development and Applications of Bioluminescent and
876 Chemiluminescent Reporters and Biosensors. *Annu. Rev. Anal. Chem. (Palo Alto. Calif).*
877 **12**, 129–150 (2019).
878 14. Welsh, J. P., Patel, K. G., Manthiram, K. & Swartz, J. R. Multiply mutated Gaussia
879 luciferases provide prolonged and intense bioluminescence. *Biochem. Biophys. Res.*
880 *Commun.* **389**, 563–8 (2009).
881 15. Kim, S. B., Sato, M. & Tao, H. Split Gaussia luciferase-based bioluminescence template
882 for tracing protein dynamics in living cells. *Anal. Chem.* **81**, 67–74 (2009).
883 16. Saito, K. *et al.* Luminescent proteins for high-speed single-cell and whole-body imaging.
884 *Nat. Commun.* **3**, 1262 (2012).
885 17. Chen, T.-W. *et al.* Ultrasensitive fluorescent proteins for imaging neuronal activity. *Nature*
886 **499**, 295–300 (2013).
887 18. Suzuki, K. *et al.* Five colour variants of bright luminescent protein for real-time multicolour
888 bioimaging. *Nat. Commun.* **7**, 13718 (2016).
889 19. Oh, Y. *et al.* An orange calcium-modulated bioluminescent indicator for non-invasive
890 activity imaging. *Nat. Chem. Biol.* **15**, 433–436 (2019).
891 20. Farhana, I., Hossain, M. N., Suzuki, K., Matsuda, T. & Nagai, T. Genetically Encoded
892 Fluorescence/Bioluminescence Bimodal Indicators for Ca(2+) Imaging. *ACS sensors* **4**,
893 1825–1834 (2019).
894 21. Motta-Mena, L. B. *et al.* An optogenetic gene expression system with rapid activation and
895 deactivation kinetics. *Nat. Chem. Biol.* (2014) doi:10.1038/nchembio.1430.
896 22. Berndt, A., Yizhar, O., Gunaydin, L. A., Hegemann, P. & Deisseroth, K. Bi-stable neural
897 state switches. *Nat. Neurosci.* **12**, 229–34 (2009).
898 23. Berglund, K., Fernandez, A. M., Gutekunst, C. A. N., Hochgeschwender, U. & Gross, R.
899 E. Step-function luminopsins for bimodal prolonged neuromodulation. *J. Neurosci. Res.*
900 **98**, 422–436 (2020).
901 24. Prakash, M. *et al.* Selective control of synaptically-connected circuit elements by all-
902 optical synapses. *Commun. Biol.* **5**, 33 (2022).
903 25. Govorunova, E. G., Sineshchekov, O. A., Janz, R., Liu, X. & Spudich, J. L. Natural light-
904 gated anion channels: A family of microbial rhodopsins for advanced optogenetics.
905 *Science (80-.).* **349**, 647–50 (2015).
906 26. Prakash, M., Medendorp, W. E. & Hochgeschwender, U. Defining parameters of
907 specificity for bioluminescent optogenetic activation of neurons using in vitro multi
908 electrode arrays (MEA). *J. Neurosci. Res.* **98**, 437–447 (2020).
909 27. Hochbaum, D. R. *et al.* All-optical electrophysiology in mammalian neurons using
910 engineered microbial rhodopsins. *Nat. Methods* **11**, 825–833 (2014).
911 28. Yang, J. *et al.* Coupling optogenetic stimulation with NanoLuc-based luminescence
912 (BRET) Ca(++) sensing. *Nat. Commun.* **7**, 13268 (2016).
913 29. Qian, Y., Rancic, V., Wu, J., Ballanyi, K. & Campbell, R. E. A Bioluminescent Ca(2+)

Indicator Based on a Topological Variant of GCaMP6s. *Chembiochem* **20**, 516–520 (2019).
30. Lambert, G. G. *et al.* CaBLAM! A high-contrast bioluminescent Ca(2+) indicator derived from an engineered Oplophorus gracilirostris luciferase. *bioRxiv* (2025) doi:10.1101/2023.06.25.546478.
31. Lee, D., Hyun, J. H., Jung, K., Hannan, P. & Kwon, H.-B. A calcium- and light-gated switch to induce gene expression in activated neurons. *Nat. Biotechnol.* **35**, 858–863 (2017).
32. Wang, W. *et al.* A light- A nd calcium-gated transcription factor for imaging and manipulating activated neurons. *Nat. Biotechnol.* **35**, 864–871 (2017).
33. O'Neill, B. K. & Laughlin, S. T. Neuronal Calcium Recording with an Engineered TEV Protease. *ACS chemical biology* vol. 13 1159–1164 at https://doi.org/10.1021/acschembio.8b00130 (2018).
34. Merolla, A. *et al.* A pH-sensitive closed-loop nanomachine to control hyperexcitability at the single neuron level. *Nat. Commun.* **15**, 5609 (2024).
35. Novitskaya, Y., Sara, S. J., Logothetis, N. K. & Eschenko, O. Ripple-triggered stimulation of the locus coeruleus during post-learning sleep disrupts ripple/spindle coupling and impairs memory consolidation. *Learn. Mem.* **23**, 238–248 (2016).
36. Lustenberger, C. *et al.* Feedback-Controlled Transcranial Alternating Current Stimulation Reveals a Functional Role of Sleep Spindles in Motor Memory Consolidation. *Curr. Biol.* **26**, 2127–2136 (2016).
37. Paz, J. T. *et al.* Closed-loop optogenetic control of thalamus as a tool for interrupting seizures after cortical injury. *Nat. Neurosci.* **16**, 64–70 (2013).
38. Gomez-Ramirez, M., More, A. I., Friedman, N. G., Hochgeschwender, U. & Moore, C. I. The BioLuminescent-OptoGenetic in vivo response to coelenterazine is proportional, sensitive, and specific in neocortex. *J. Neurosci. Res.* **98**, 471–480 (2020).
39. Hodneland, E., Kögel, T., Frei, D. M., Gerdes, H.-H. & Lundervold, A. CellSegm - a MATLAB toolbox for high-throughput 3D cell segmentation. *Source Code Biol. Med.* **8**, 16 (2013).
40. Ludwig, K. A. *et al.* Using a common average reference to improve cortical neuron recordings from microelectrode arrays. *J. Neurophysiol.* **101**, 1679–1689 (2009).

Acknowledgments
We would like to thank all members of Bioluminescence Hub laboratories for their feedback, discussions, and thoughtful comments throughout the progression of this work. (http://www.bioluminescencehub.org/)

Competing interests
The authors have no conflicts of interest to declare.

Author contributions
Conceptualization, AP, ELC, NCS, CIM, UH; Validation, AP, ELC, CIM, DL, NCS, UH; Formal Analysis, AP, ELC; Investigation, AP, ELC, MP, ADS, ZZ, MG-R, MOT; Data Curation, AP, ELC; Writing—Original Draft, AP, ELC; Writing—Review & Editing, ELC, NCS, CIM, UH; Visualization, AP, ELC; Supervision, CIM, NCS, UH; Project Administration, UH; Funding Acquisition, CIM, DL, NCS, UH.

Funding
This work was supported by National Institutes of Health grants R21MH101525, R21EY026427, U01NS099709, National Science Foundation grants CBET-1464686, DBI-1707352, and the W.M. Keck Foundation.

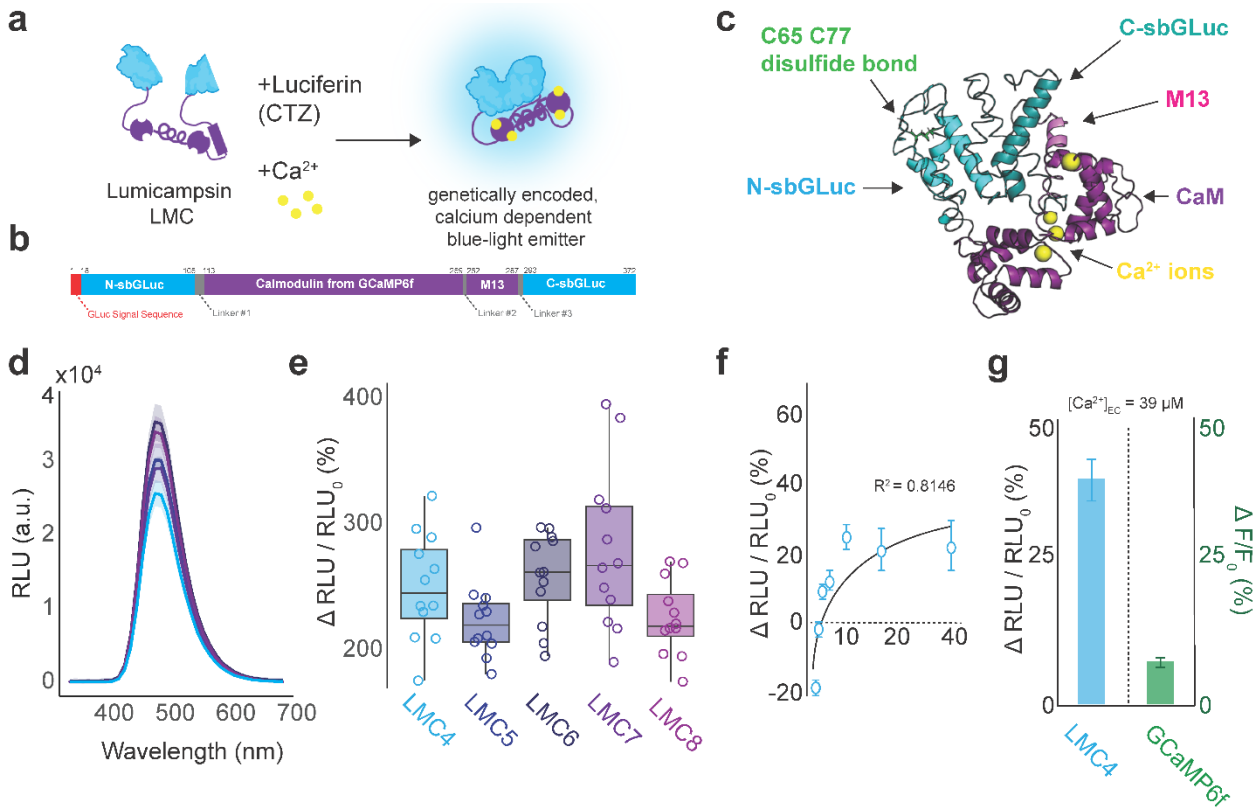

Figure 1. **Design of a *Gaussia* luciferase based Ca^{2+} sensor. a**. sbGLuc (light blue) is split by a CaM–M13 module (purple), producing a dim basal signal in the presence of its luciferin (CTZ). Binding of Ca^{2+} (yellow) reconstitutes an active luciferase and increases light emission in the presence of luciferin. **b**. Elements of the coding sequence for LMC: *Gaussia* luciferase signal peptide (red), N- and C-terminal fragments of sbGLuc (light blue), calmodulin sequence from GCaMP6f (purple), M13 sequence (purple), and various linker regions (gray). **c.** Structure model of LMC. **d.** Emission wavelength across LMC variants (4-8; for color code see e.). The LMC constructs were transiently expressed in HeLa cells and light emission after luciferin and histamine addition was measured across the wavelength spectra (data presented as mean ± SEM). **e.** Change in luminescence in the presence of luciferin in response to 10 μM histamine in HeLa cells across LMC variants (N=12 wells per sensor, Unpaired *t*-test was used to determine *p*-values, corrected for multiple comparisons with Holm-Šídák method: LMC4 vs LMC5: *P*=0.3712; LMC4 vs LMC6: *P*=0.6193; LMC4 vs LMC7: *P*= 0.3977; LMC4 vs LMC8: *P*= 0.3712). Boxplots show median, 25th and 75th percentiles (box edges), whiskers to most extreme data points, and individual outliers. **f.** Percent change in bioluminescence in HEK293 cells expressing LMC4 in response to 2 μM ionomycin under increasing extracellular Ca^{2+} concentrations. Cells were pre incubated with 5 μM luciferin and varying concentrations of Ca^{2+}; acute Ca^{2+} flux was initiated by injection of ionomycin before photon counting in a luminometer (mean ± s.e.m). **g.** Response of LMC4 and GCaMP6f to acute Ca^{2+} flux. HEK293 cells expressing LMC4 or GCaMP6f were held in 39 μM extracellular Ca^{2+} concentration and ionomycin was added to 2μM final concentration. LMC4 expressing HEK cells were pre-incubated with CTZ at 5 μM final concentration. Bioluminescence readings for LMC4 were taken on a SpectraMax-L luminometer and fluorescent images for GCaMP6f were taken on a Zeiss AxioObserver A1 microscope with a Hamamatsu Ocra Flash4.0 CMOS camera before and after the addition of ionomycin. Graph displays percent change in signal before and after ionomycin induced Ca^{2+} flux (mean ± SEM).

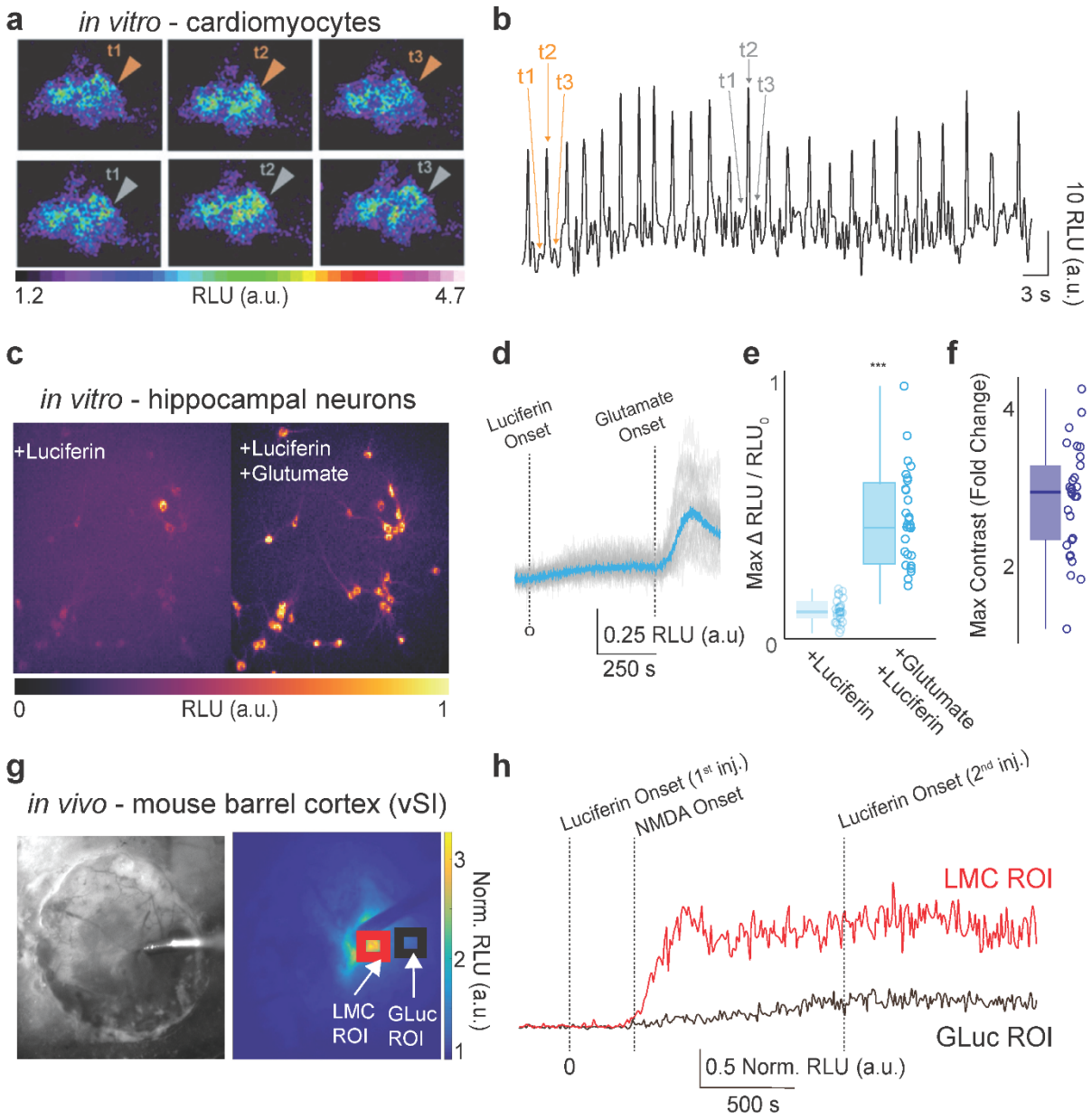

Figure 2. Reporting Ca^{2+} flux *in vitro* and *in vivo*. a. Primary cardiomyocytes nucleofected with LMC and incubated with luciferin (100 µM CTZ). Pseudocolored images show regions of interest (ROIs) at three time points (t1–t3) before and after ATP (10 µM) application. **b.** Representative bioluminescence traces from the ROIs in (a). Orange and grey arrows mark the time points corresponding to t1–t3 in (a). **c.** Representative hippocampal neurons expressing LMC imaged with luciferin alone (left) or with luciferin and glutamate (right). **d.** Mean (blue) overlaid with individual bioluminescence traces (grey) of LMC responses to bath-applied luciferin and glutamate. **e.** Box plot showing maximal luminescence responses (Max $\Delta RLU/RLU_0$) of LMC-expressing cells exposed to luciferin alone or to glutamate in the presence of luciferin (N= 29 neurons from two independent cultures, Wilcoxon signed rank test: P= 2.7023 x10^{-6}). **f.** Maximum fold change (contrast) in response across neurons. **g.** *in vivo* imaging of mouse barrel cortex (vSI) expressing LMC. *left*: brightfield image showing injection site. *right:* Relative luminescence heatmap with ROIs for LMC (red) and control GLuc (black). Luciferin (CTZ, 50 µL) was delivered via the lateral ventricle, and NMDA (1 µL) was applied directly to cortex. **h**. Comparison of bioluminescence emission over area transduced with Ca^{2+} dependent luciferase, AAV-LMC4f (red box in image, red line in graph) versus area transduced with non-Ca2+ responsive luciferase, AAV-GLuc (black box in image, black line in graph). Representative traces from ROIs in (g) showing luminescence after luciferin (CTZ) and NMDA delivery. Onset of CTZ and NMDA injections are indicated. Boxplots show median, 25th and 75th percentiles (box edges), whiskers to most extreme data points, and individual outliers.

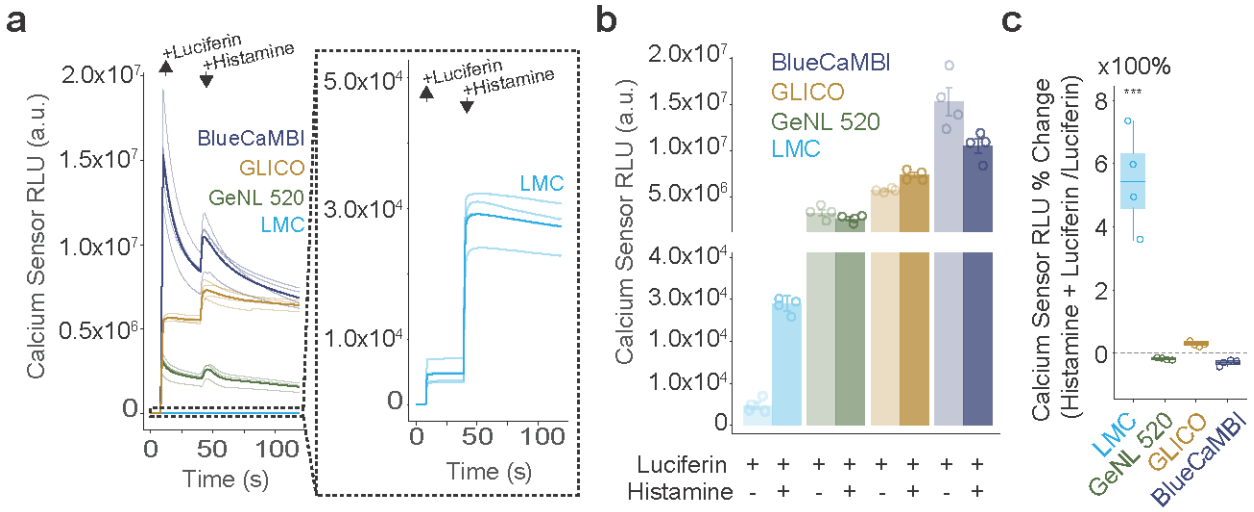

Figure 3. Integrating Ca^{2+} flux with activation of photoreceptors. a. Luminometer time series from HeLa cells transiently expressing BlueCaMBI, GLICO, GeNL, or LMC following addition of luciferin and histamine. Inset shows LMC traces on an extended scale. **b.** Peak bioluminescence measured after luciferin and histamine stimulation for each sensor from (a). **c.** Histamine-specific percent change in bioluminescence normalized to luciferin baseline, expressed as percent change for each calcium sensor. (N=4 wells/sensor, LMC vs GLICO: P= 4.65x10^{-6}, GeNL: P= 5.51x10^{-7}, BlueCAMBI: P= 1.46x10^{-6}; GeNL vs GLICO P= 0.38, BlueCAMBI P= 0.996; BlueCAMBI vs GLICO: P=0.723, Tukey's post hoc multiple-comparison's test following a one-way analysis of variance (ANOVA), $F_{(3, 12)}$ **=** 48.56, P**=** 5.51x10^{-7}). Boxplots show median, 25th and 75th percentiles (box edges), whiskers to most extreme data points, and individual outliers.

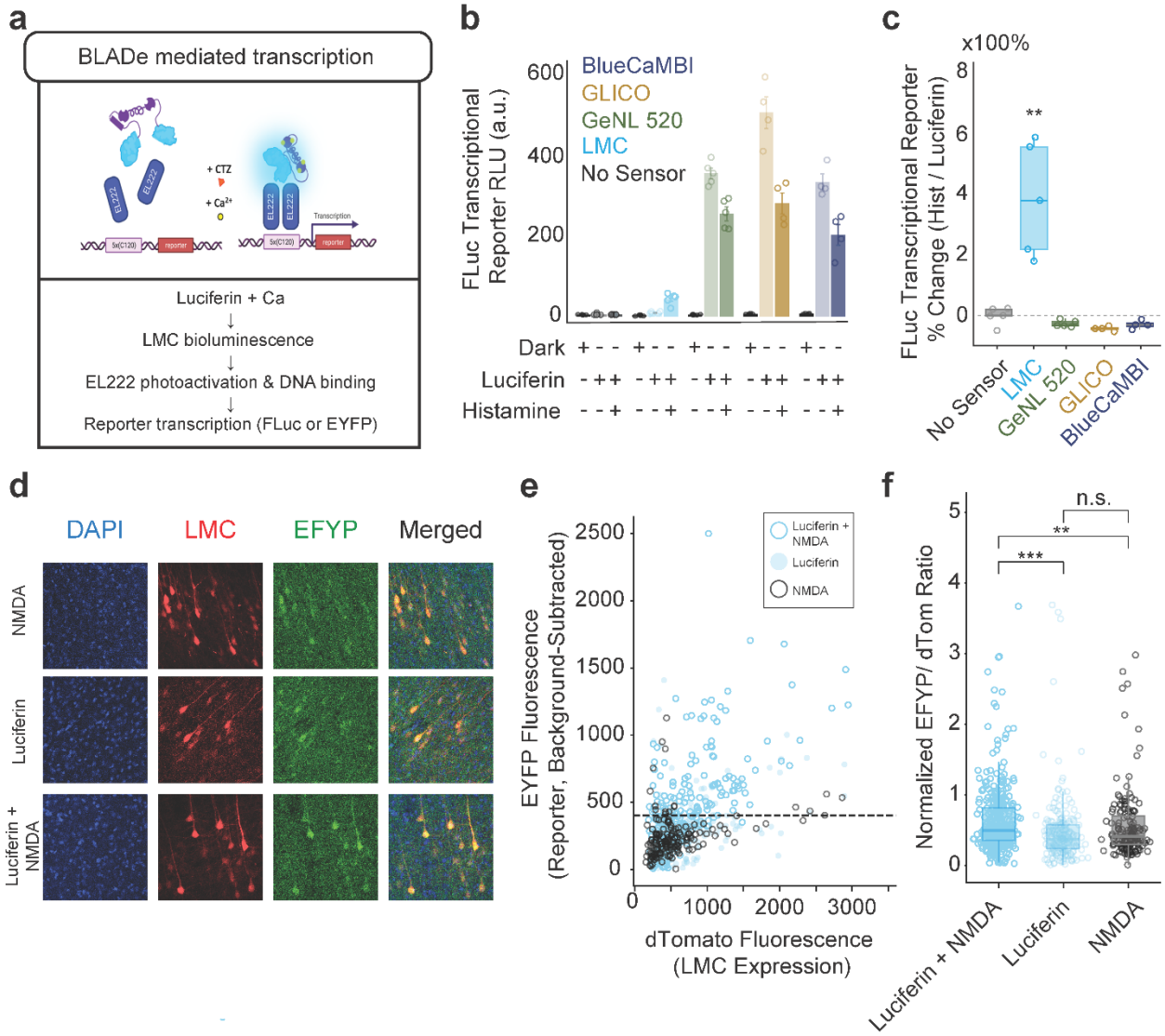

Figure 4. Converting intracellular activity to transcription. a. Schematic of LMC leading to bioluminescence mediated dimerization of the light sensing transcription factor EL222 in the presence of Ca^{2+} and luciferin (CTZ). The photoactivated EL222 homodimer then binds to the promoter 5xC120 and leads to transcription of the reporter gene. **b.** Firefly luciferase (FLuc) transcriptional reporter measured under dark, luciferin-only, or luciferin + histamine treatments in HeLa cells transiently expressing BlueCaMBI, GLICO, GeNL, or LMC. **c.** FLuc transcriptional reporter normalized to luciferin baseline expressed as percent change for each sensor/condition. **d.** Representative confocal images showing EYFP transcriptional reporter (green), LMC P2A-tdTomato viral expression (red), and nuclear DAPI stain (blue) from a field of view in mouse prefrontal cortex following intraventricular injection of luciferin and/or NMDA. Mixtures of AAV9 preparations of the 3 constructs were stereotaxically injected into the medial prefrontal cortex of mice. Three or more weeks later mice received injections of NMDA alone, CTZ alone, or CTZ and NMDA. Brains were collected 18 hours later and sections imaged under a confocal microscope. **e.** EYFP reporter expression quantified as per-cell EYFP/tdTomato ratio across treatment groups. Each point represents a single cell derived from three treatment groups: Luciferin-NMDA (N= 350 cells/2 mice), Luciferin-ONLY N= 197 cells/2 mice), NMDA-ONLY (N= 147 cells/2 mice). Dotted line indicates the 90th percentile EYFP/dTomato ratio observed in the NMDA-ONLY group, used as a threshold to define transcriptional activation above baseline. **f.** EYFP reporter intensity plotted against tdTomato fluorescence for each cell and condition. Boxplots show median, 25th and 75th percentiles (box edges), whiskers to most extreme data points, and individual outliers.

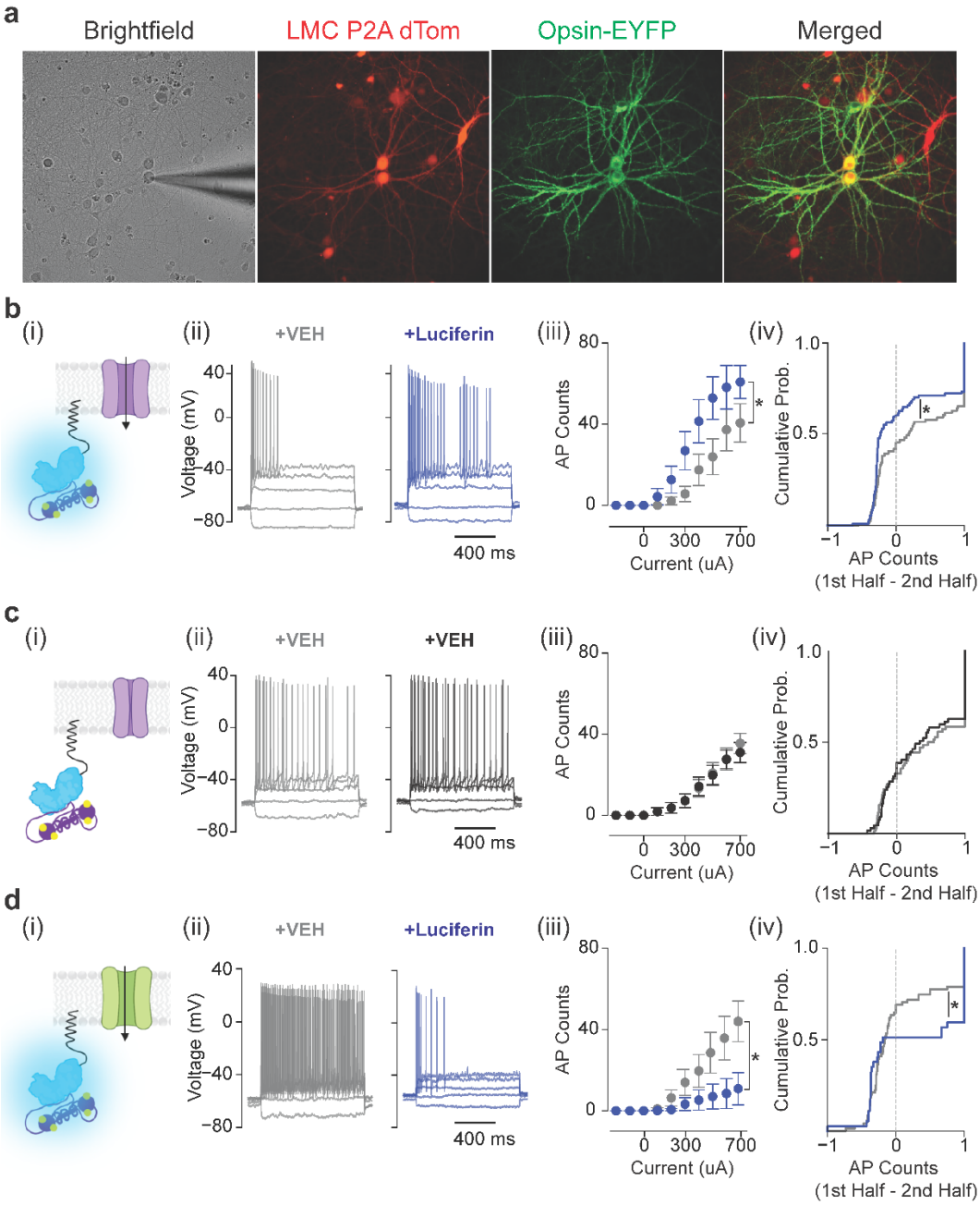

Figure 5. Integrating Ca^{2+} flux with change in membrane potential in single neurons *in vitro*. a. Brightfield and fluorescence images of cultured cortical neurons nucleofected with opsin (ChR2(C128S))-EYFP and LMC-P2A-dTomato and used for whole-cell patch-clamp recordings. The patch electrode is visible in the brightfield image. **b.** (i) Schematic of farnesylated LMC anchored to the inner cell membrane near the excitatory opsin ChR2(C128S) enabling light-mediated activation in the presence of depolarization-induced Ca^{2+} flux and the luciferin (CTZ). (ii) Representative membrane voltage responses to step current injections before (gray) and after (blue) bath perfusion of luciferin in a neuron co-expressing LMC and ChR2(C128S). (iii) Action potential counts under vehicle (gray) and luciferin (blue) conditions. Data expressed as mean ± SEM. (iv) Empirical cumulative distribution of spike fraction changes across voltage traces for vehicle and luciferin conditions, represented as the difference in spike counts between the first and second halves of the recording. **c.** (i) Schematic of a control condition, where LMC is co-expressed with ChR2(C128S) in the presence of Ca^{2+} but without luciferin, preventing light-mediated activation. (ii–iv) Same analyses as in b. **d.** (i) Schematic of LMC co-expressed with the inhibitory opsin hGtACR2, enabling light-mediated suppression of activity in the presence of Ca^{2+} and luciferin. (ii–iv) Same analyses as in b, showing inhibition rather than activation. Data are presented as mean ± SEM in panels.

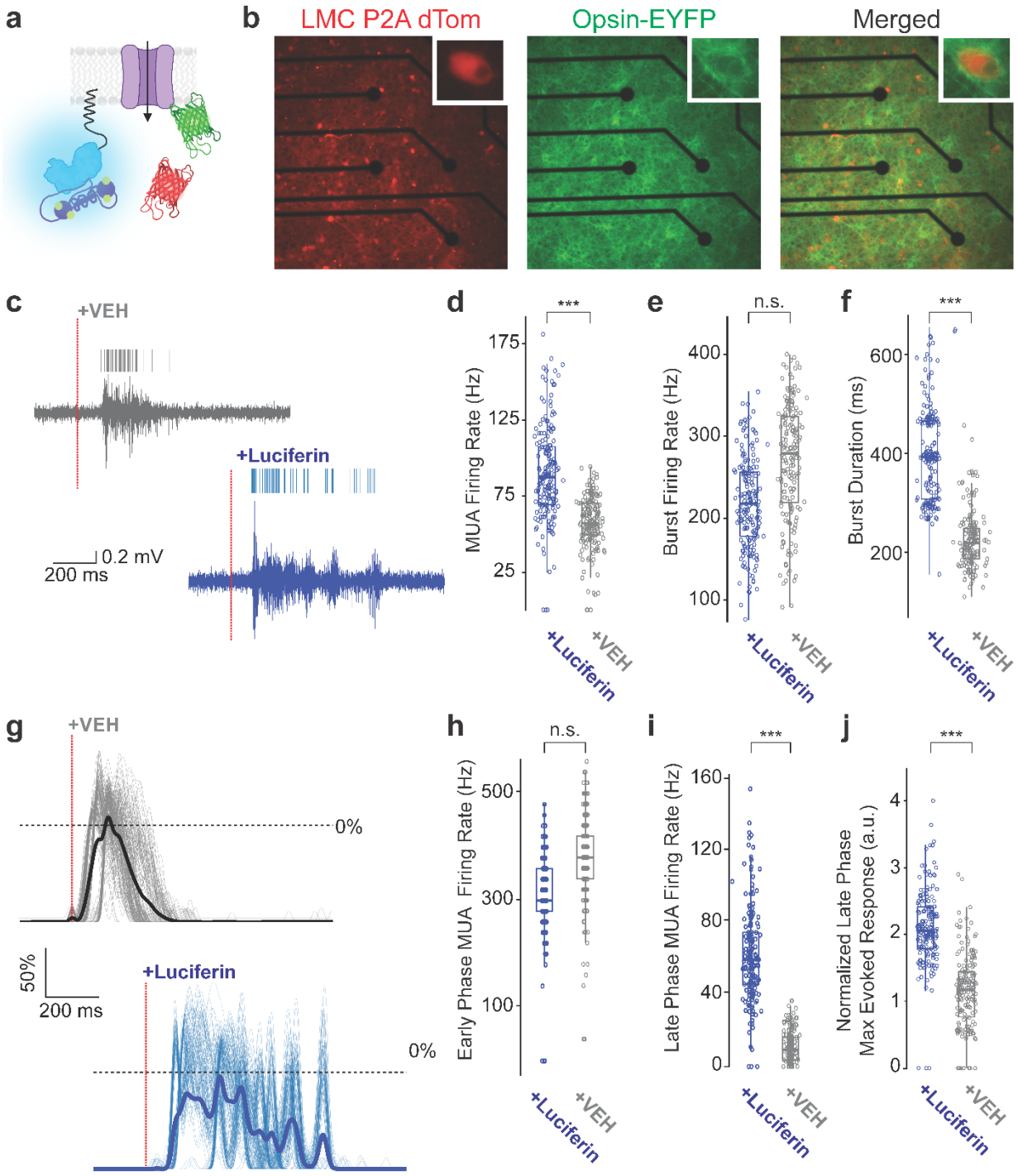

Figure 6. Integrating Ca^{2+}+ flux with change in membrane potential in neural populations *in vitro*. a. Schematic of farnesylated LMC anchored to the inner cell membrane near the excitatory opsin ChR2(C128S) enabling light-mediated activation in the presence of depolarization-induced Ca^{2+} flux and the luciferin (CTZ). **b.** Fluorescence images of cultured cortical neurons co-transduced with LMC-P2A-dTomato (red) and ChR2(C128S)-EYFP (green). **c.** Representative filtered voltage traces from one channel before and after vehicle (top) or luciferin (bottom) application. Red dashed line indicates time of application. **d.** MUA firing rate was increased in the luciferin condition (Wilcoxon signed-rank test, $P = 3.93 \times 10^{-28}$, Holm-corrected). **e.** Burst rate was not significantly different between luciferin and vehicle conditions (Wilcoxon signed-rank test, $P = 0.63$, Holm-corrected). **f.** Burst duration was significantly prolonged in the luciferin condition (Wilcoxon signed-rank test, $P = 3.18 \times 10^{-49}$, Holm-corrected). **g.** Time-aligned MUA traces

across all electrodes showing normalized population responses following vehicle (top) or luciferin (bottom) application. Individual electrode traces are shown in grey (vehicle) and blue (luciferin); thick lines represent the mean response per condition. MUA was smoothed using a sliding 5-point boxcar window. **h.** Early-phase (0–50 ms) MUA firing rates following application was not different between luciferin and vehicle (Wilcoxon signed-rank test, P= 0.13, Holm-corrected). **i.** Late-phase (150–1000 ms) MUA firing rate was significantly higher in the luciferin condition (Wilcoxon signed-rank test, P= 2.61×10^{-8}, Holm-corrected). **j.** Late phase normalized MUA was significantly increased under luciferin (Wilcoxon signed-rank test, P= 1.02×10^{-11}, Holm-corrected). For **d-f** and **h-j**, N=57-59 pairs of electrodes per recording pooled across three independent MEA cultures. Boxplots show median, 25th and 75th percentiles (box edges), whiskers to most extreme data points, and individual outliers.

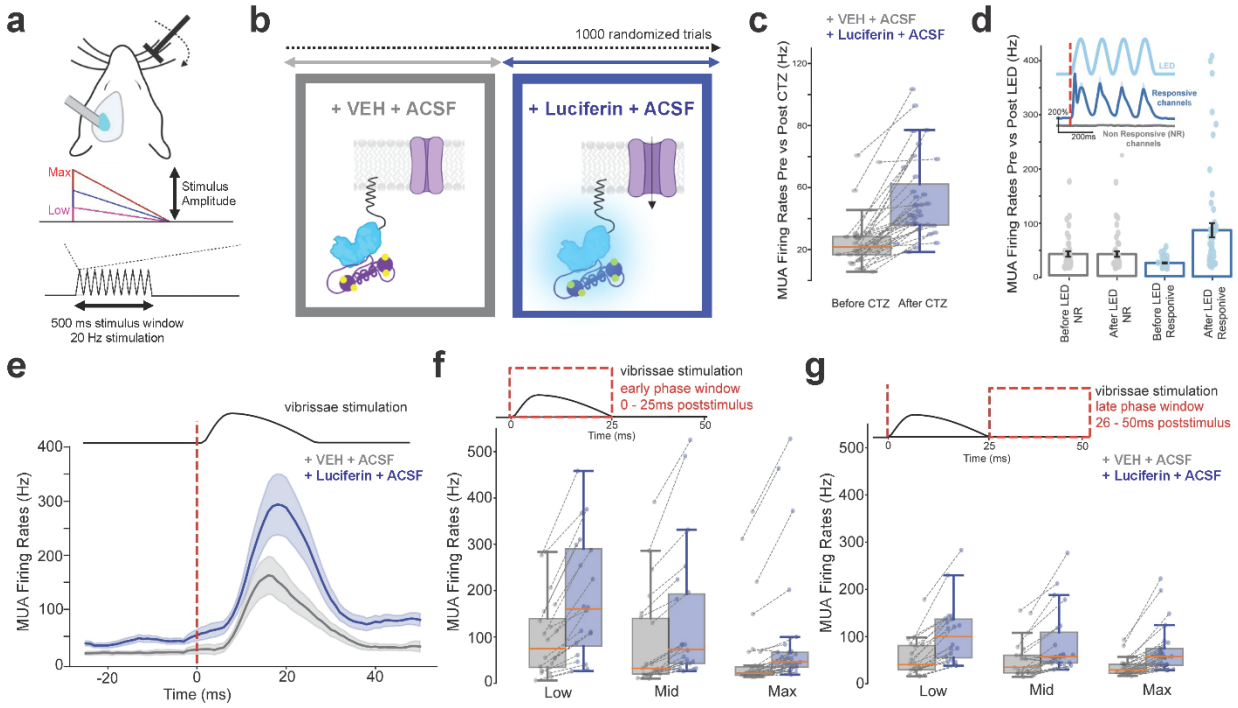

Figure 7. Integrating spontaneous and sensory inputs into changes in firing rates *in vivo*. a. Schematic of the experimental design. Extracellular electrophysiology recordings from SI barrel cortex during varied vibrissal deflections (zero, low, mid, max intensities) for 500ms at 20Hz. **b**. Schematic of the experimental timeline. Each recording consisted of 1000 trials (~2.5 hour sessions) where ACSF containing vehicle or CTZ was constantly perfused over the craniotomy. During each treatment epoch, vibrissal deflections were randomly presented. In the presence of the sensory stimulus and vehicle (grey box), there is no activity dependent light emission of LMC. In contrast, in the presence of CTZ and the sensory stimulus (blue box), sensory recruitment leads to activity dependent bioluminescence and subsequently photoactivation of opsins in neurons. **c**. MUA firing rate before and after the bath application of CTZ over the craniotomy. **d.** MUA firing rates for responsive and non-responsive channels to optogenetic stimulation. *Inset:* the pattern LED signal (teal), percent change of firing rate for responsive (blue) and non-responsive channels (grey). **e.** Peristimulus time histograms from two distinct recording sites reflect changes in spiking activity evoked by contralateral sensory driven recruitment during the vehicle (grey) and CTZ (blue) treatment periods during low amplitude vibrissae stimulation. **f.** Mean multiunit activity responses to vibrissae stimulation during the early phase window, vehicle (grey) vs CTZ (blue) epoch as a function of low, medium, and max vibrissae stimulus amplitude. *inset:* schematic of the analog signal controlling the piezo stimulator, red box is the window of time where the mean was quantified. **g.** Same as (f), but during the late phase window. All data are plotted as mean +/- SEM.

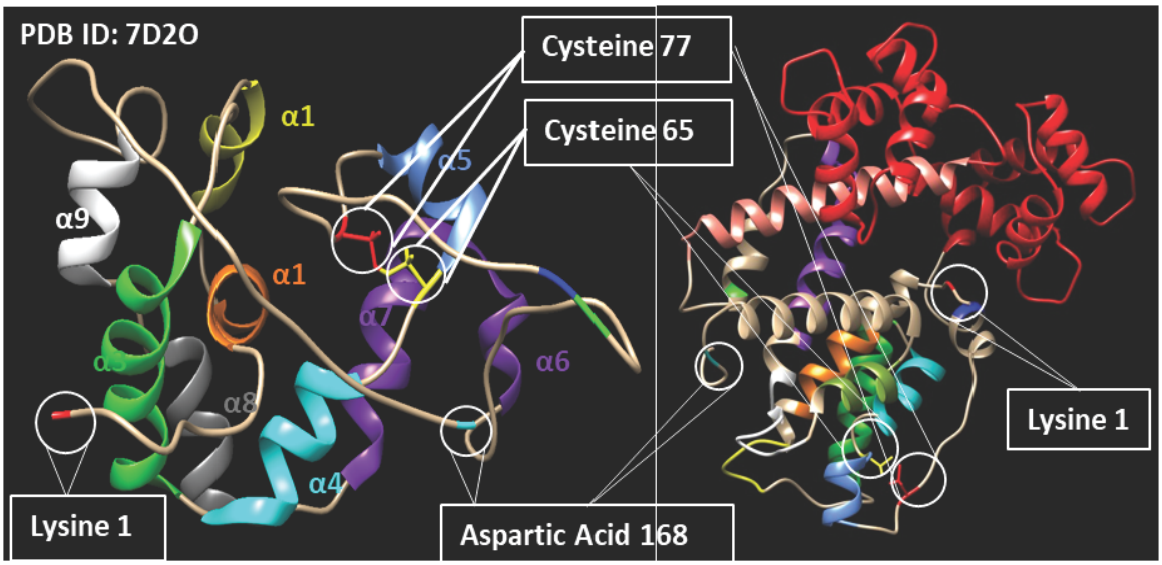

Supplemental Figure S1. Ribbon diagrams of GLuc indicating 9 alpha helices. Left: Of the 9 alpha helices α4 and α7 form the most rigid block of the luciferase stabilized by a disulphide bond between Cysteine 65 and 77. Right: The Calcium sensing moiety, CaM-M13 was inserted between Q88 and G89. In its unbound state, the CaM-M13 destabilizes the C65-C77 disuphide bond just by pushing the two halves away from each other. When bound to Ca^{2+}, the CaM-M13 pulls on both halves and stabilizes the C65-C77 disulphide bond to render the luciferase functional.

a

sbGluc(M43L_M110L):

K[1]PTENNEDFNIVAVASNFATTDLDADRGKLPGKKLPLEVLKELEANARKAGCTRGCLIC
LSHIKC[65]TPKMKKFIPGRC[77]HTYEGDKESAQ[88]G[89]GIGEAIVDIPEIPGFKDLEPLEQF
IAQVDLCVDCTTGCLKGLANVQCSDLLKKWLPQRCATFASKIQGQVDKIKGAGGD[168]

b

LMC4: Signal Sequence; Gluc N half; CaM-M13; Gluc C half; Alpha Helix; Linker

**MGVKVLFALICIAVAEAK[1]PTENNEDFNIVAVASNFATTDLDADRGKLPGKKLPLEVLKELE
ANARKAGCTRGCLICLSHIKC[65]TPKMKKFIPGRC[77]HTYEGDKESAQ[88]GGGGTMADQLTEE
QIAEFKEEFSLFDKDGDGTITTKELGTVMRSLGQNPTEAELQDMINEVDADGDGTIDFPEF
LTMMARKMKYRDTEEEIREAFGVFDKDGNGYISAAELRHVMTNLGEKLTDEEVDEMIREAD
IDGDGQVNYEEFVQMMTAKGGKRRWKKNFIAVSAANRFKKISSSGAL GSGGGG[89]GIGEAIV
DIPEIPGFKDLEPLEQFIAQVDLCVDCTTGCLKGLANVQCSDLLKKWLPQRCATFASKIQG
QVDKIKGAGGD[168]**

Supplemental Figure S2. Amino acid sequences of sbGLuc and LMC4. **a**. Amino acid sequence of sbGLuc with landmark mutations of sbGLuc versus wildtype GLuc color coded. **b**. Amino acid sequence of LMC4 with landmarks indicated by colors and underlines.

a

LMC Linker-CaM-M13 Comparisons

```
LMC4 1    GGGGTMADQLTEEQIAEFKEEFSLFDKDGDGTITTKELGTVMRSLGQNPTEAELQDMINEVDADGDGTIDFPEFLTMMAR  80
LMC5 1    GGGGTLPDQLTEEQIAEFKEAFSLFDKDGDGTITTKELGTVMRSLGQNPTEAELQDMINEVDADGDGTIDFPEFLTMMAR  80
LMC6 1    GGGGTLPDQLTEEQIAEFKEAFSLFDKDGDGTITTKELGTVMRSLGQNPTEAELQDMINEVDADGDGTIDFPEFLTMMAR  80
LMC7 1    GGGGTMHDQLTEEQIAEFKEAFSLFDKDGDGTITTKELGTVMRSLGQNPTEAELQDMINEVDADGNGTIYFPEFLTMMAR  80
LMC8 1    GGGGTMHDQLTEEQIAEFKEAFSLFDKDGDGTITTRELGTVMRSLGQNPTEAELQDMINEVDADGNGTIYFPEFLTMMAR  80

LMC4 81   KMKYRDTEEEIREAFGVFDKDGNGYISAAELRHVMTNLGEKLTDEEVDEMIREADIDGDGQVNYEEFVQMMTAKGGKRRW  160
LMC5 81   KMKYRDTEEEIREAFGVFDKDGNGYISAAELRHVMTNLGEKLTDEEVDEMIREADIDGDGQVNYEEFVQMMTAKGGKRRW  160
LMC6 81   KGSYRDTEEEIREAFGVFDKDGNGYISAAELRHVMTNLGEKLTDEEVDEMIREADIDGDGQVNYEEFVQMMTAKGGKRRW  160
LMC7 81   KMKDTDSEEEIREAFRVFDKDGNGYISAAQLRHVMTNLGEKLTDEEVDEMIREADIDGDGQVNYEEFVQMMTAKGGKRRW  160
LMC8 81   KMKDTDSEEEIREAFRVFDKDGNGYISAAQLRHVMTNLGVKLTDEEVDEMIREADIDGDGQVNYEEFEQMMTAKGGKRRW  160

LMC4 161  KKNFIAVSAANRFKKISSSGALGSGGG  187
LMC5 161  KKNFIAVSAANRFKKISSSGALGSGGG  187
LMC6 161  KKNFIAVSAANRFKKISSSGALGSGGG  187
LMC7 161  KKNFIAVSAANRFKKISSSGALGSGGG  187
LMC8 161  KKNFIAVSAANRFKKISSSGALGSGGG  187
```

Supplemental Figure S3. Different variants of Lumicampsin (LMC) based on different calmodulin moieties. **a**. All LMC derivatives have the same sbGluc split between residues Q88 and G89 and the same M13 moiety with different calmodulin moieties inserted: GCaMP6f (Chen et al., 2013; LMC4), GCaMP6s (Chen et al., 2013; LMC5), GCaMP6m (Chen et al., 2013; LMC6), Ca^{2+}-NL (Saito et al., 2012; LMC7), Ca^{2+}-eNL (Suzuki et al., 2016; LMC8). Dark blue font indicates amino acids varying between the five versions.

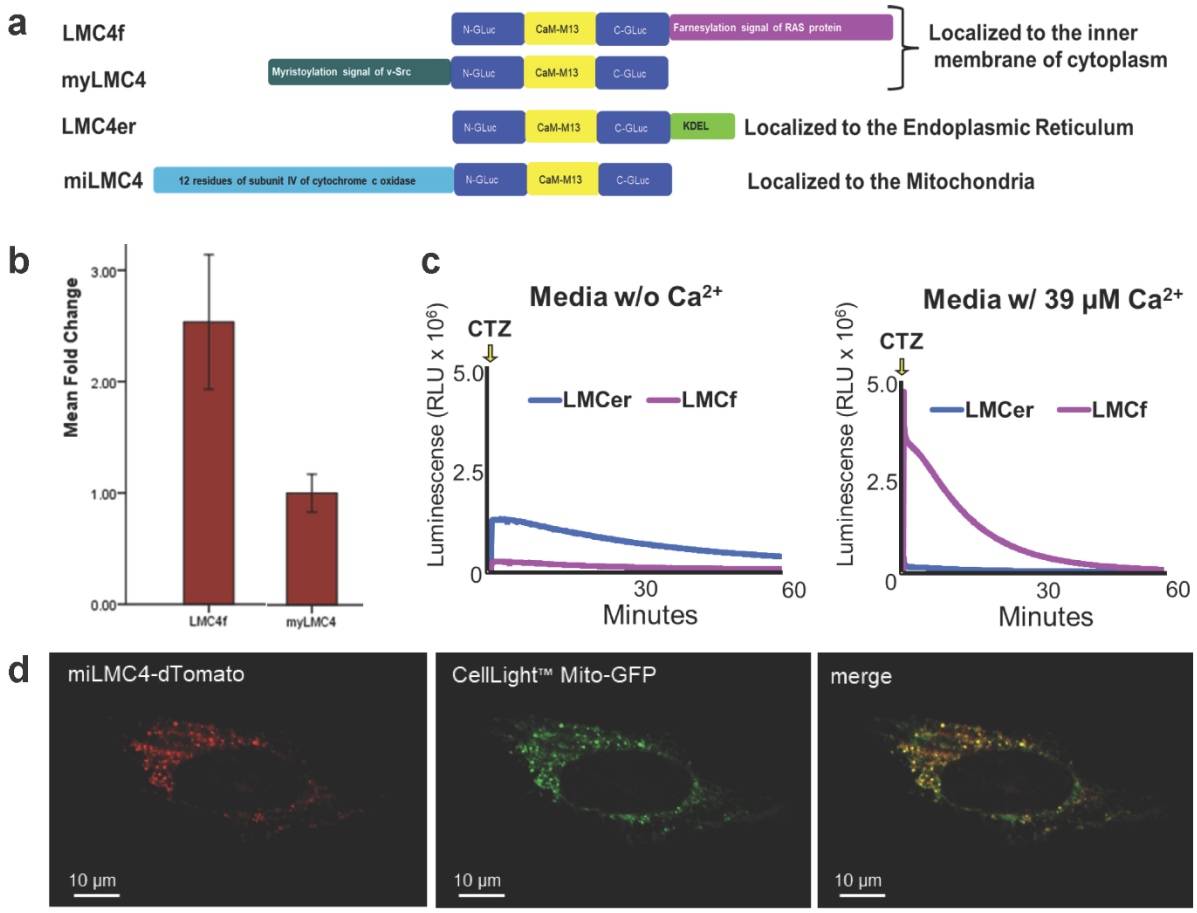

Supplemental Figure S4. Different versions of LMC4 based on different subcellular targeting sequences. **a**. Schematics of four versions of LMC4 targeting the Ca2+ sensor to the inner cell membrane via a farnesylation or myristoylation signal, to the ER via a KDEL signal, or to the mitochondrial membrane via a mitochondrial targeting signal of cytochrome c oxidase. **b**. Mean fold change of light emission from HeLa cells expressing LMC4f or myLMC4 after histamine-induced Ca2+ flux. **c**. Bioluminescence response to ionomycin induced Ca^{2+} flux in HEK293 cells expressing LMC4f or LMC4er in the presence of CTZ and in the absence or presence of extracellular Ca^{2+}. **d**. Confocal images of HeLa cells expressing miLMC4-dTomato and BacMam2.0-Mito-GFP.

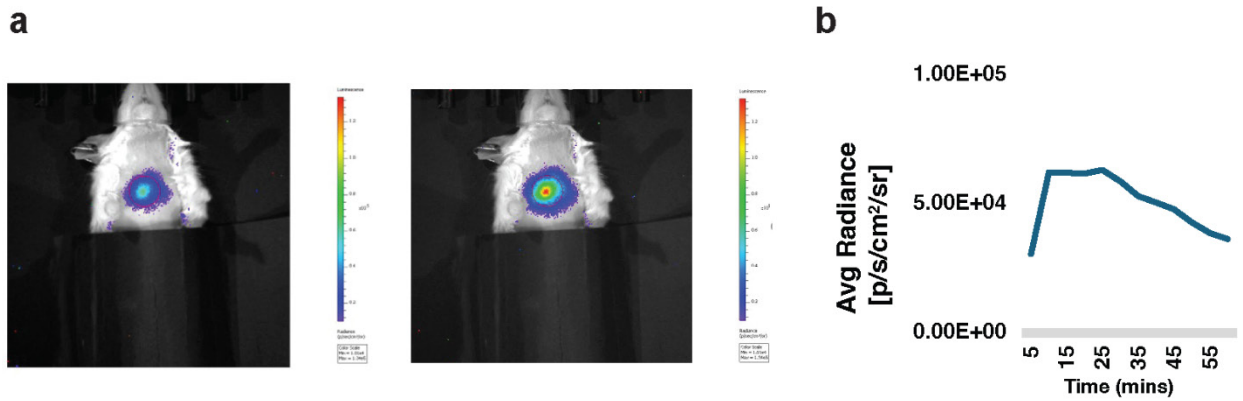

1167

1168 **Supplementary Figure S5. LMC reports Ca^{2+} flux in cardiomyocytes *in vivo*. a.**Pseudocolored IVIS images
1169 showing bioluminescent signal from a mouse heart transduced with AAV2/9-CAG-LMC4f. Images correspond to
1170 baseline (left) and peak signal (right) following intraperitoneal injection of 100 µg water-soluble luciferin (CTZ). **b.** Peak
1171 signal was reached approximately 15 minutes post-injection and is plotted in the accompanying time course graph
1172 (right).

1173

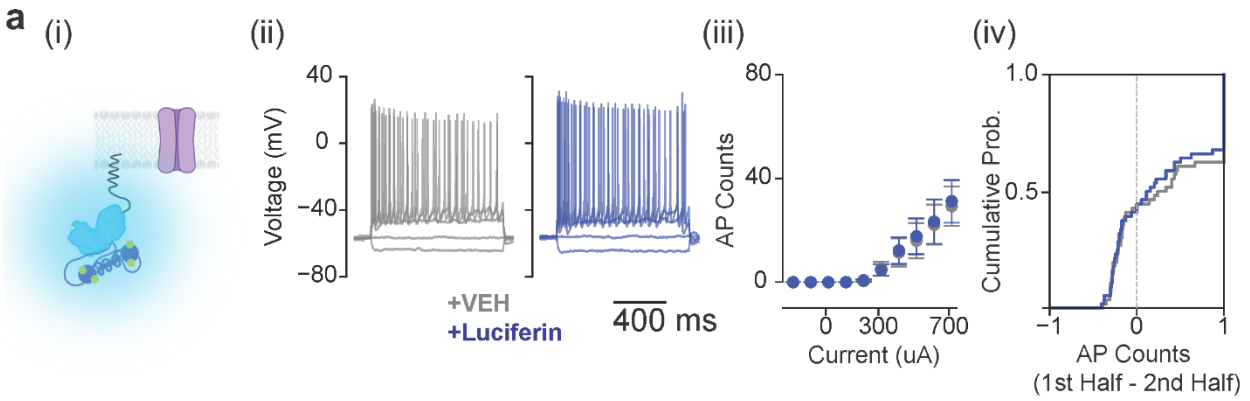

Supplementary Figure S6. Lack of BLADe-mediated changes in neurons expressing a non-functional "DUD" opsin. (i) Schematic of farnesylated LMC anchored to the inner cell membrane near the non-functional DUD opsin, showing that in the presence of depolarization-induced Ca^{2+} flux and luciferin (CTZ), no light-mediated modulation is expected. (ii) Representative membrane voltage responses to step current injections before (gray) and after (blue) bath perfusion of luciferin in a neuron co-expressing the DUD opsin and LMC, showing no change in firing. (iii) Action potential counts under vehicle (gray) and luciferin (blue) conditions remain similar. (iv) Empirical cumulative distribution of spike fraction changes across voltage traces for vehicle and luciferin conditions, demonstrating no shift in spike timing (Kolmogorov-Smirnov test, KS= 0.0545, *P*= 0.999) or firing rate in the absence of a functional opsin. Data expressed as mean ± SEM from N=6 neurons.

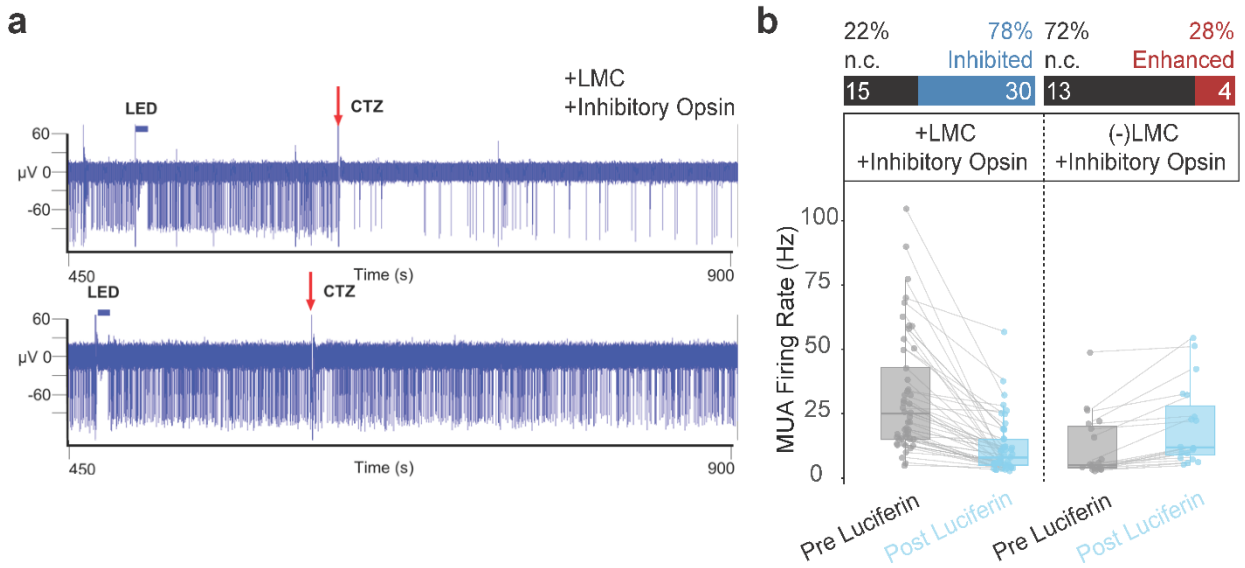

Supplementary Figure S7. LMC enables light-dependent suppression of cortical network activity via an inhibitory opsin. a. Representative multi-unit activity (MUA) traces from cortical neurons recorded on multielectrode arrays. Neurons co-expressing LMC and the inhibitory opsin hGtACR2 (top) show reduced spiking following luciferin (CTZ) addition (red arrow). In contrast, neurons expressing the opsin alone (bottom) show no consistent change in firing after CTZ. **b.** Quantification of firing rate changes before and after luciferin addition across individual electrodes. n.c., no change in firing; inhibited, decrease in firing; enhanced, increase in firing

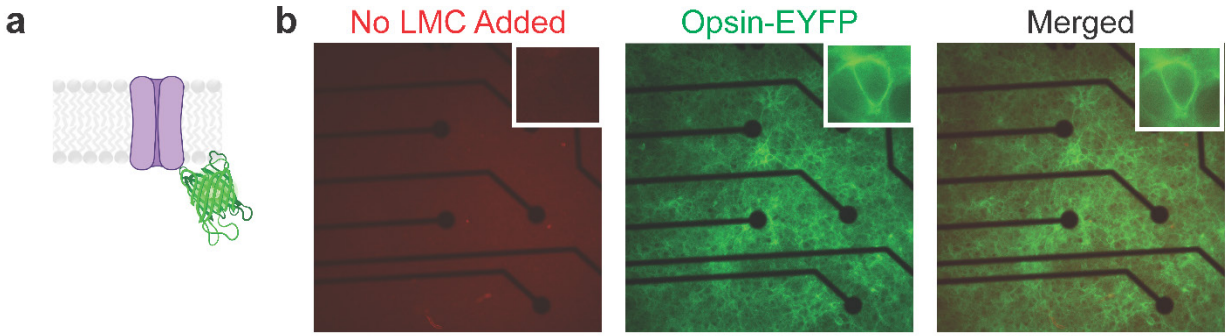

Supplementary Figure S8. MEA co-expression control: opsin-only cultures lack LMC. a. Schematic of multi-electrode array (MEA) setup with an opsin-expressing neuron positioned above the recording site. **b.** Fluorescence images of a representative opsin-only culture showing absence of dTomato signal (left, red channel) and strong opsin-EYFP expression (middle, green channel). Merged image (right) confirms that these neurons express the opsin but not LMC. Insets show magnified views of cell bodies overlaying electrode contacts. These cultures serve as a negative control for luciferin-dependent changes in network activity.

1203 **Supplementary Table 1. List of plasmids**

1204

Plasmid	Source
pcDNA3.1-CMV-LMC4-P2A-dTomato	This paper
pcDNA3.1-CMV-LMC5-P2A-dTomato	
pcDNA3.1-CMV-LMC6-P2A-dTomato	
pcDNA3.1-CMV-LMC7-P2A-dTomato	
pcDNA3.1-CMV-LMC8-P2A-dTomato	
pcDNA3.1-CMV-LMC4f-P2A-dTomato	
pcDNA3.1-CMV-myLMC4-P2A-dTomato	
pcDNA3.1-CMV-LMC4er-P2A-dTomato	
pcDNA3.1-CMV-miLMC4-P2A-dTomato	
pcDNA3.1-CMV-GCaMP6f	
pcDNA3.1-CMV-BlueCaMBI	
pcDNA3.1-CMV-GLICO	
pcDNA3.1-CMV-ChR2(C128S)-EYFP	
pcDNA3.1-CMV-hGtACR2-EYFP	
pcDNA3.1-CMV- ChR2(C128S)-E97R-D253A	
pcDNA3.1-5xC120-EYFP	
pAAV-hSyn-LMC4f-P2A-dTomato	
pAAV-CAG-VP-EL222	
pAAV-5xC120-EYFP	
pAAV-Efla-DIO-CheRiff-EYFP	
pAAV-Efla-DIO-LMC4f-P2A -dTomato	
pcDNA3.1-CAG-VP-EL222	Kevin Gardner, CUNY
pcDNA3.1-5xC120-FireflyLuc	Kevin Gardner, CUNY
pcDNA3-CMV-GeNL(Ca2+)_520	Addgene plasmid # 85204
pAAV.Syn.GCaMP6f.WPRE.SV40	Addgene plasmid # 10083
pFUGW-hGtACR2-EYFP	Addgene plasmid # 67877
pLenti-CaMKIIa-hChR2(C128S)-EYFP-WPRE	Addgene plasmid # 20294
pAAV-hsyn-CheRiff-eGFP	Addgene plasmid # 51697

1205

1206